Effects of Powder Reuse on The Mechanical Properties of Electron Beam Additively Manufactured Ti-6Al-4V

Reid Schur

A thesis submitted in partial fulfillment of the requirements for the degree of

Master of Science

University of Washington

2019

Committee:

Dwayne Arola

Ramulu Mamidala

Lucien Brush

Program Authorized to Offer Degree:

Materials Science and Engineering

University of Washington

Abstract

Effects of Powder Reuse on The Mechanical Properties of Electron Beam Additively Manufactured Ti-6Al-4V

Reid Schur

Chair of the Supervisory Committee:

Dwayne Arola

Department of Materials Science and Engineering

Metal Additive Manufacturing (AM) shows incredible promise for small batch, highly customizable part production. Powder bed fusion systems build parts layer by layer from metal powder that is manufactured according to stringent requirements, including chemistry, sphericity and particle size distribution. To maximize process economy, there is interest in reusing powder from inside the build chamber that is heat cycled but is not integrated into the fused metal. This practice can reduce process waste and lower material costs. However, the powder undergoes thermal cycling during printing and mechanical damage as a result of powder recovery. There has been limited investigation concerning the quality of metal that results from AM with reused powder. In order for recovered powder to be used for stress- or mission-critical engineering applications, the effect of powder reuse on the mechanical properties must be understood. In this investigation, the quality of Ti-6Al-4V metal developed in AM by electron beam melting was evaluated as a function of powder recovery and reuse in subsequent build cycles. The printed metal quality was characterized in terms of profilometry, mechanical properties that result from tensile testing, and fractographic evaluation of the fractured tensile specimens.

Results showed that there are many aspects of the metal quality that are influenced by powder reuse in EBM of Ti-6Al-4V. Regarding the external surface quality of the built components, the average and ten-point surface roughness (Ra and Rz, respectively) decreased linearly with powder reuse. The mechanical properties also showed substantial dependence on reuse, but the tends were dependent on the orientation of the metal with regards to the build orientation. Regardless of build orientation, the elastic modulus, yield strength, ultimate tensile strength, and strength coefficient of the metal all increased linearly. There was a minor decrease in the strain hardening exponent. However the % elongation decreased significantly with reductions in the % elongation of 61.9% and 37.1%, in the horizontal and vertical build orientations, respectively. Fractography revealed a transition from ductile to brittle features with powder reuse, and also provided insight into the defects present that contributed to changes in the ductility. These included small spherical voids,

lack of fusion voids, and cracks. Based on these findings, the preferred orientation for stress-critical AM parts of Ti-6Al-4V is in the vertical direction.

The metal anisotropy represented by the differences in mechanical properties of the horizontally and vertically oriented parts is likely due to the texture in the microstructure. Complimentary work on the microstructure of the Ti-6Al-4V shows that the metal has columnar prior β grains oriented parallel to the build direction with α/β basketweave structure between them. The prior β grain boundaries could serve in pinning dislocations when loading is perpendicular to their orientation, thereby leading to lower strain to fracture of the horizontal specimens. However, the largest contribution to the changes in mechanical properties with powder reuse are related to increasing oxidation content of the powder during recovery. Interstitial oxides serve to strengthen and embrittle the material. The results achieved herein should contribute to the development of guidelines on powder reuse in EBM additive manufacturing of Ti-6Al-4V.

Table of Contents

1. Introduction

1.1 Additive Manufacturing

Additive manufacturing (AM) has historically been used for rapid prototyping of components. By utilizing polymeric mediums, realistic models could be created with nothing more than a CAD file and a spool of plastic wire. While their mechanical properties were insufficient for most applications, their ease of creation and low cost made them ideal for prototyping. With the advent of metal additive manufacturing, it became more realistic to use additively manufactured components in demanding engineering applications. Additive manufacturing holds a number of benefits over traditional manufacturing techniques (casting, machining, etc.) that make it extremely desirable. AM can create net shape parts without the need for molds or machining. This allows a single machine to manufacture an endless variety of parts, allowing for low-cost, one-off or limited-run production. Customizable parts become possible at costs low costs. AM also avoids many of the limitations on manufacturable geometries present with machining and

casting. Complex shapes and internal cavities unimaginable with conventional manufacturing become possible with AM.

Metals can be additively manufactured by a variety of methods. There are powder bed fusion systems (PBF) that fill a chamber with metal powder layer-by-layer, selectively melting sections for the parts, as well as wire fed systems (directed energy deposition, DED). Some systems use lasers to melt the metal, while others use electron beams. Each type of printer has its benefits and limitations. One of the more exciting classes of printers is the powder bed system. Compared with DED, PBF systems can achieve significantly higher resolution.

Within additive manufacturing, powder bed fusion systems create more waste than DED systems. During the printing process the entire build envelope is filled with powder, even though the printed components occupy only a portion of the envelope, resulting in wasted powder. Ti-6Al-4V powder suitable for AM is expensive to manufacture; the required powder size distribution and purity needed for high quality parts raises the price of an already expensive base material. As a result, it has become common practice to reuse the powder from the build chamber, lowering manufacturing costs and reducing waste. The powder in the build chamber does not remain in pristine condition, however; it undergoes thermal and mechanical damage through use, and the effect of powder reuse on mechanical properties must be understood before this process can be adopted in industry for critical parts.

1.2

2. Evolution of Mechanical Properties of AM Parts with Powder Reuse

2.1 Introduction

An assessment of the effects of powder reuse on mechanical properties and microstructure of additively manufactured Ti-6Al-4V components is critical to evaluating the potential of reusing powder for commercial aerostructures. Optimizing the degree of powder reuse can provide an economic advantage as long as the mechanical properties remain within performance expectations and the material exhibits targeted reliability. In this section, the methods and results from mechanical testing are presented and discussed. This work is one of three complementary areas of analysis. The other two, microstructure and chemistry/defect analysis, are referenced at times. Any necessary data is included in the Appendices.

2.2 Materials and Methods

2.2.1 Arcam A2X Printer

The Arcam A2X platform was used in this study. This is a PBF system that utilizes an electron beam to sinter and fuse the powder. The build chamber must be operated under vacuum to prevent scattering of the electron beam. The system and a schematic of the interior are shown in Figure 1.

Figure 1: Arcam A2X (a) and a schematic of the interior (b).

The machine operates with 4 basic steps: preheat, powder raking, sintering, and selective melting. These steps are summarized below.

1. Preheat

The preheat occurs at the start of the print process. The chamber temperature is raised to approximately 700°C. Holding the base plate at this temperature results in a cooling rate of the melted metal that prevents the formation of brittle α' martensite, forming a more ductile α/β lamellar structure instead [1]. It also eliminates the need for a stress relief heat treatment, a process needed in laser melt systems.

2. Powder Raking

After the preheat, powder is pushed onto the build plate in an even layer approximately 50 μm thick. The thickness of these layers is on the same scale as the powder diameter, allowing for the highest resolution possible.

3. Sintering

Next the electron beam is rastered across the powder surface, lightly sintering the powder together. This prevents movement of the powder during melting from electrostatic interactions caused by the electron beam.

4. Selective Melting

Finally, the powder is selectively melted. The electron beam fuses powder for the parts. The beam begins by outlining these areas, called a contour pass. Next, the beam fills in the interior of these shapes, rastering according to hatching patterns defined in the printer settings. Finally, any support structures needed (as defined by the user) are melted. Steps 2-4 are repeated until printing is complete.

The Arcam A2X allows the user to define a large number of processing parameters. Arcam provides preset settings optimized for Ti-6Al-4V which were used for the duration of the experiment, summarized in Appendix B.

1.3 Powder Recovery System

A separate powder reclamation system (PRS) is available from Arcam for the A2X (Appendix B) which was used in this study. The block of sintered powder containing the parts is removed from the printer and transferred to the PRS. Inside the glove box, the block is blasted with Ti-6Al-4V powder to break apart the sintered powder and expose the printed parts. The sintered powder can be collected, sieved to remove large particles, and then reused in the printer.

2.2.1 Raw Material

The alloy used in these experiments is Ti-6Al-4V. It is a common aerospace alloy utilized for its high strength-to-weight ratio, corrosion resistance, heat treatability, and retention of mechanical properties at elevated temperatures. These traits make Ti-6Al-4V an excellent engineering material for aerospace applications. Wrought form Ti-6Al-4V must exhibit at minimum the properties seen in Table 1 [2]. The minimum mechanical properties for additively manufactured Ti-6Al-4V as specified by ASTM are lower than the wrought form, although Arcam claims their AM components can match the properties of wrought form Ti-6Al-4V [3],[4].

Table 1: Properties of Ti-6Al-4V from wrought form, ASTM AM requirements, and Arcam AM.

	Elastic Modulus (GPa)	Yield Strength (MPa)	Ultimate Tensile Strength (MPa)	% Elongation (%)
ASTM Wrought Form	120	860	930	10
ASTM AM	120	825	895	10
Arcam	120	950	1020	14

The Ti-6Al-4V stock was a gas atomized powder manufactured by AP&C, a subsidiary of GE. The gas atomization process entails spraying high pressure argon gas into a stream of molten

metal [5]. The liquid metal separates into tiny droplets that solidify into metal powder. The powder was qualified by Arcam to verify that its chemical composition and particle size distribution fall within expected ranges. The certificate of analysis is found in Appendix A.

2.2.2 Standard Build

A standard set of specimens outlined in Figure 2 was printed (referred to as a build from here on, where the first print using virgin powder is b1). The specimens include 6 vertical tensile specimens, 6 horizontal tensile specimens, 2 staircases and a cylindrical pyramid for microstructure evaluation, and a small cylinder for micro-CT porosity assessment.

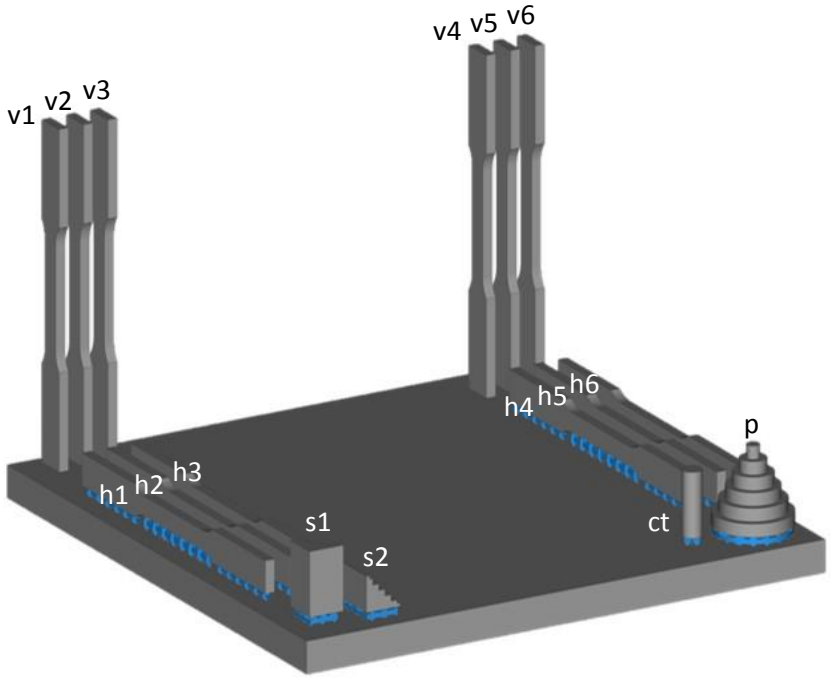

Figure 2: Layout of the build chamber, containing vertical tensile specimens (v1-v6), horizontal tensile specimens (h1-h6), microstructural analysis specimens (s1, s2, p), and the micro-CT specimen (ct).

The tensile specimens were used to assess mechanical properties. The specimens were created according to ASTM E08 and follow the subsize rectangular specimen specifications [6]. These

specimens were printed in two orientations, the vertical and horizontal directions as seen in Figure 2. The dimensions of the tensile specimens are illustrated in Figure 3.

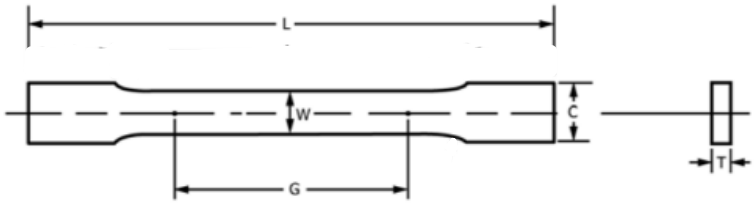

Figure 3: Tensile specimen dimensions, which include L = 104 mm, W = 6 mm, G = 25 mm, C = 10 mm, T = 3 mm.

2.2.3 Powder Reuse

The experiment began with 50 kg of powder in virgin condition. During a build, approximately 11.9 kg of powder was used to fill the build chamber, while only ~0.16 kg of that was fused to create all the specimens. The ~11.7 kg of reclaimed powder was sieved and mixed uniformly back into the unused powder in the hoppers. This mixture of reused and virgin powder was then used to print the second build (b2). This process was repeated for a total of 30 builds. In each successive build, the ratio of reused to virgin powder increased to the point that by b15, statistically all the powder should have been reused at least once, although much of the powder had been reused multiple times.

2.2.4 Profilometry

Profilometry was performed using a Keyence VR-3100 (Appendix C). The VR-3100 is a non-contact optical imager that allows for rapid analysis of surface quality over a large surface area. Profilometry was performed on three surfaces from the horizontal specimens (melt pool and both

vertical faces) and 4 surfaces from the vertical specimens (both vertical faces and both vertical edges), illustrated in Figure 4. The average of ten lines was used for the multi-line analysis. Lines were oriented along the loading direction of the tensile specimens for both horizontal and

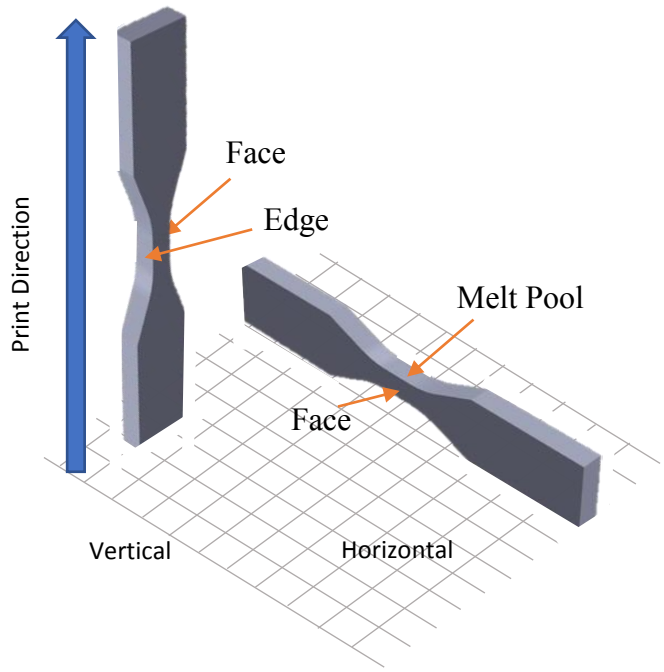

Figure 4: Locations where profilometry was performed.

vertical specimens and located in the center of the gauge section. They were 3.41 mm in length. A low pass filter of 25 μm was applied.

Examples of the line scans used are shown in Figure 5 for each of the characteristic surfaces. The build direction is noted on each of the images.

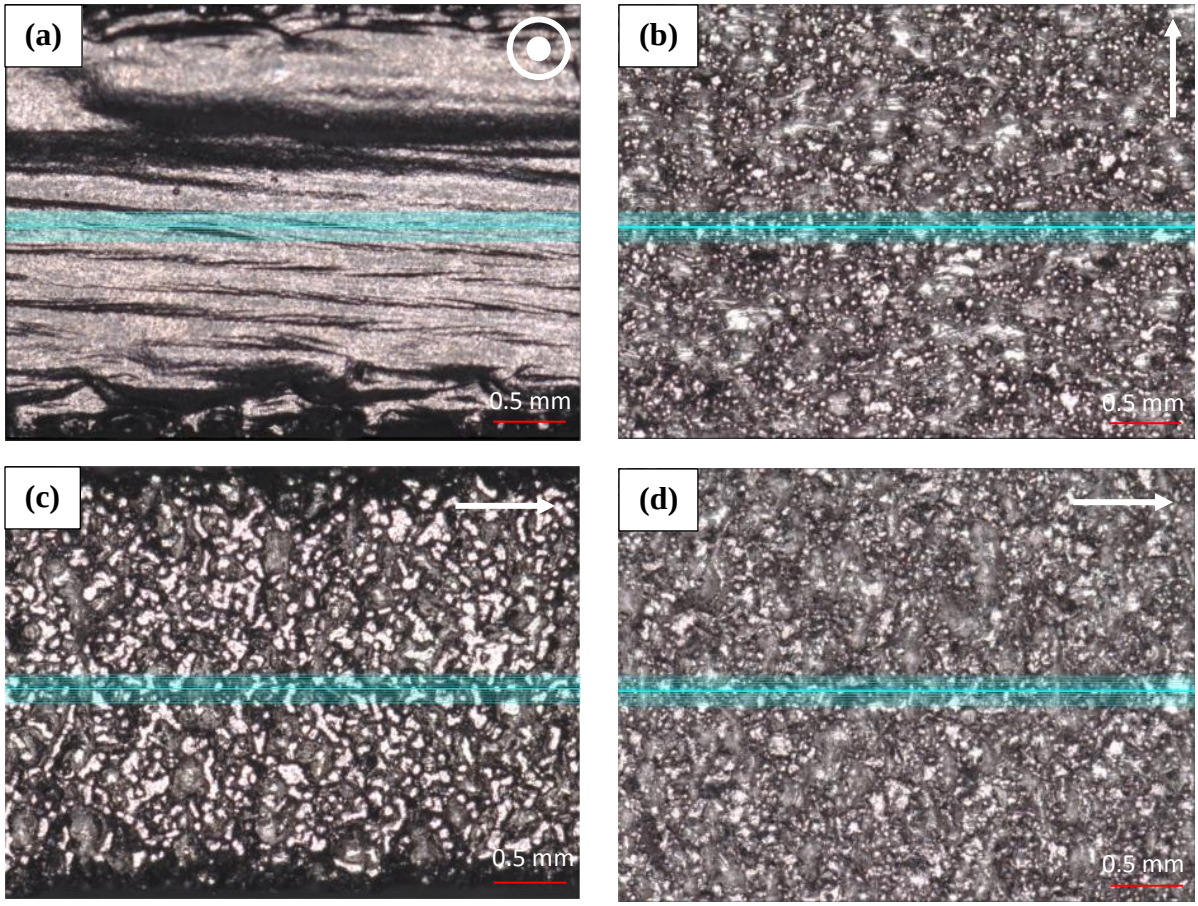

Figure 5: Locations of the lines used for multi-line profilometry of a horizontal specimen melt pool surface (a) and face (b), and vertical specimen face (c) and edge (d). Build direction is marked on each scan.

2.2.5 Tensile Testing

All tensile tests were completed according to ASTM E08, and utilized the subsize rectangular specimen geometry. A total of three vertical (v1, v3, v5) and three horizontal (h1, h3, h5) specimens were evaluated from each build. The even numbered tensile specimens were reserved for future testing. Tensile specimens were tested in the as-built condition. Other than removing the support structures on the horizontal specimens, no other surface preparation or post processing was performed. Since a main benefit of AM is its ability to create net shape parts, it is

desirable to minimize any post processing. Testing the samples in the as-built condition provides an assessment of what properties can be expected directly after printing.

The tensile tests were performed using an Instron 5585H load frame, equipped with a 50 kN load cell (Appendix C). A 250 kN load cell was used for b21-b24 due to damage to the 50 kN load cell. A displacement rate of 1.27 mm/min was used for these tests, which corresponds to a strain rate of approximately 0.0006 s^{-1}. The load and displacement data from the tensile tests were used to generate true stress-true strain curves for each specimen evaluated. The yield strength (0.2% offset), ultimate tensile strength (UTS), modulus of elasticity, % elongation (% EL), strain hardening exponent, and strength coefficient were extracted from the true stress-true strain curves. After testing, the fracture surfaces were removed for fractography.

2.2.6 Fractography

The fracture surfaces of the tensile specimens were analyzed to determine the fracture mechanisms, origins of fracture, and qualitatively assess the contribution of defects to failures. Specimens were cleaned in isopropyl alcohol and water to remove dust and other debris before analysis. Fractography was conducted using an Olympus SZX16 stereomicroscope and JEOL-6010 SEM and a Philips XL 30 SEM.

2.3 Results

Most of the builds were completed without issue. However, a few of the builds experienced partial or total failure. b2, b3, and b19 experienced build failures partway up the build height, allowing the horizontal specimens to be completed, but not the vertical specimens. These failures occurred due to vacuum problems or rake failure. b13 failed entirely. An error in the machine setup resulted in powder layers being deposited and sintered, but no melting occurred and therefore no parts were produced. The powder from this build was reused as normal. Finally, several horizontal specimens from b25, b26, b27, and b30 showed warping. Specimens b25h1, b25h3, b26h5, and b27h5 were only warped in the grip section, and were tensile tested as normal. All of these specimens failed outside the gauge section, and their data is excluded from the mechanical properties. b30h5 was too severely warped to be tested. An image of this specimen is shown below.

Figure 6: Severely warped b30h5 specimen.

2.3.1 Profilometry

The mean roughness (Ra) and ten point height (Rz) from the multi-line analysis are shown in Figure 7. These parameters are plotted versus the build number for the characteristic surfaces of the horizontal and vertical specimens. The results show that the roughness and ten point height are not affected by powder reuse. The melt pool surface Ra of the horizontal specimens is much

lower than the horizontal specimen's faces. Furthermore, any vertical surface (horizontal specimen faces, vertical specimen edge and faces) have similar Ra values, ranging from 23-37 μm. Rz values follow the same trends; the melt pool has a significantly lower value than the vertically oriented surfaces, 12-21 μm and 94-149 μm respectively.

Figure 7 –

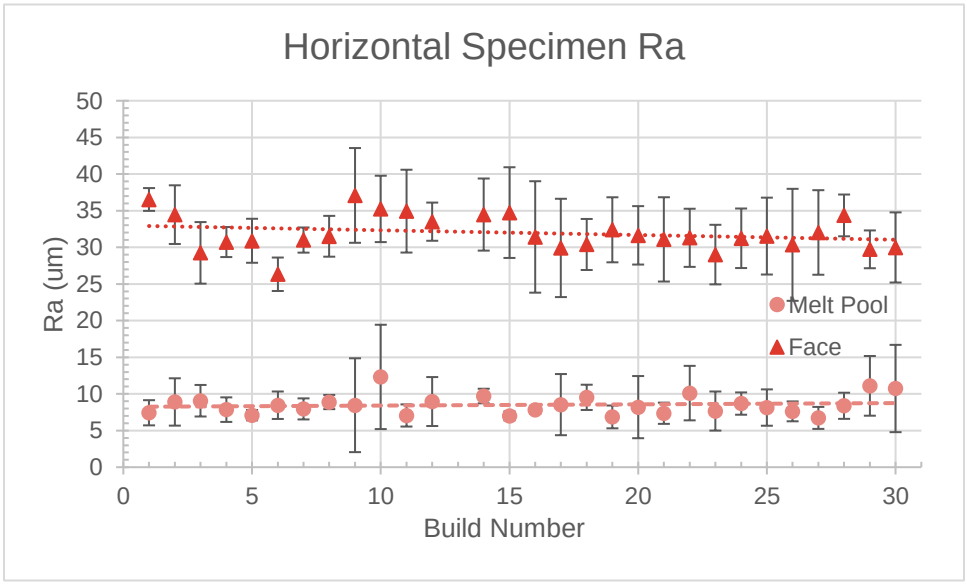

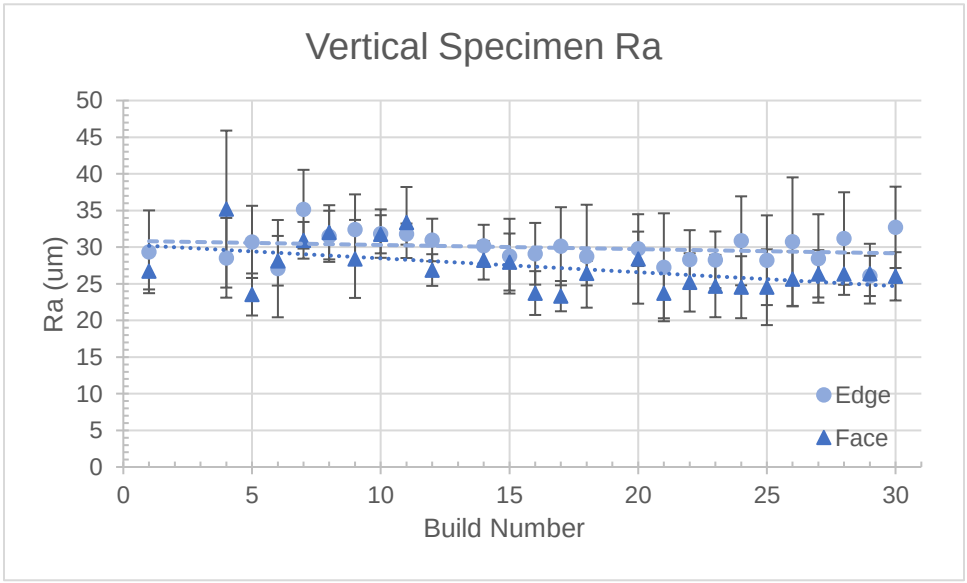

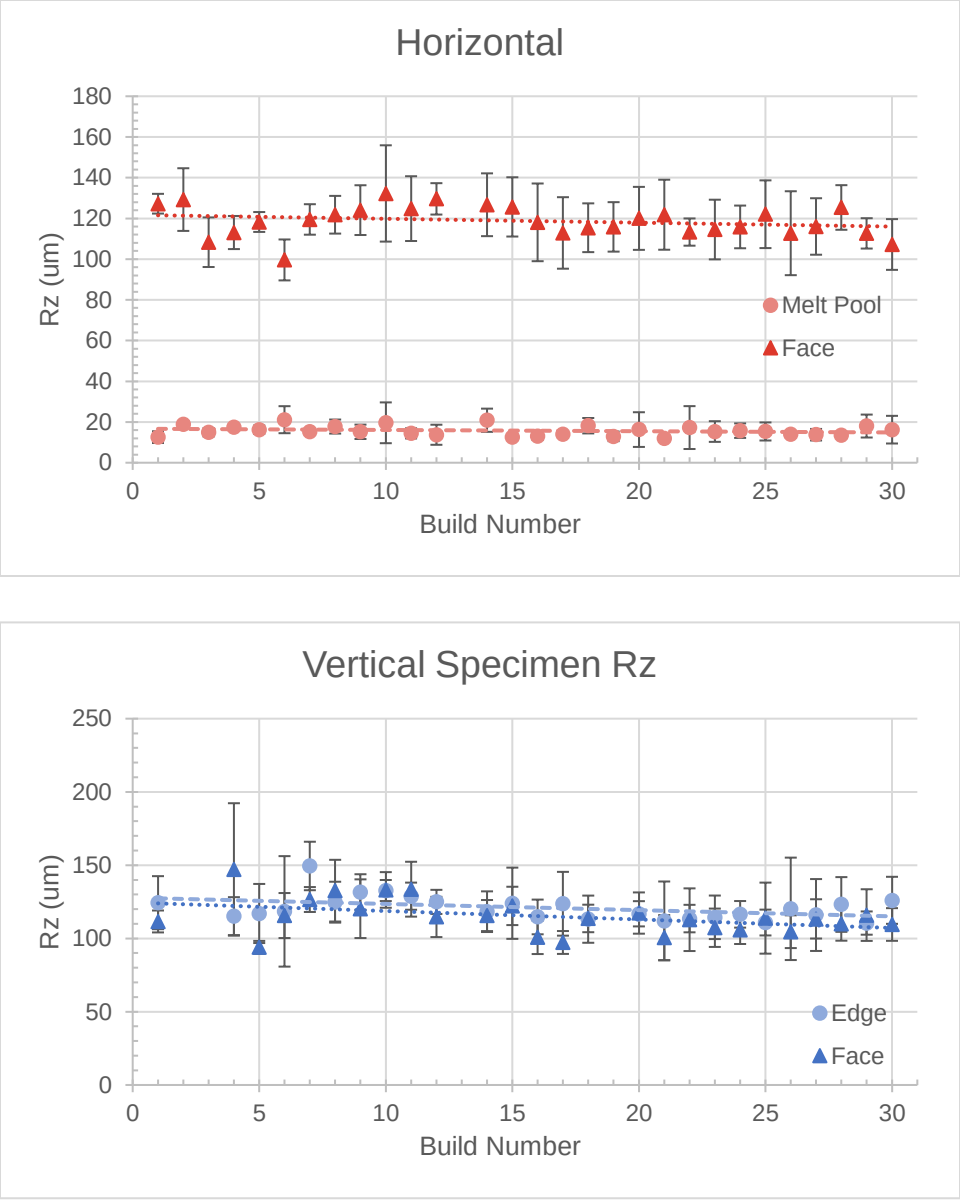

Figure 7: Ra and Rz from a multi-line analysis.

2.3.2 Tensile Testing

Load-displacement and true stress-true strain curves were generated for each tensile specimen. Representative examples from a horizontal specimen (b3h1) are shown in Figure 8. They show a standard linear elastic stress-strain response until yielding, at which point the deformation becomes plastic, leading to a small degree of necking and then failure.

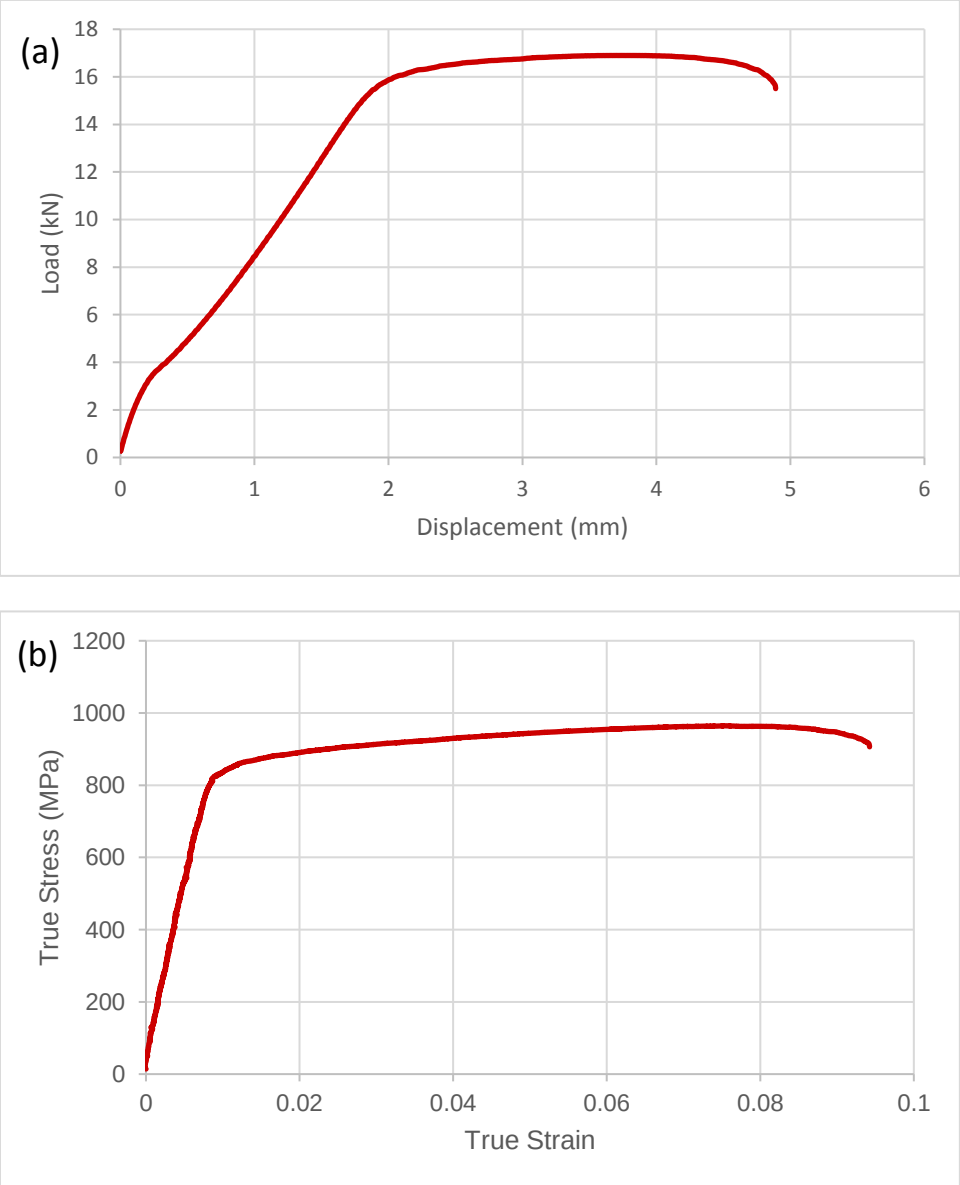

Figure 8: Load-displacement curve (a) and true stress-true strain curve (b) from a b3 horizontal specimen (b3h1).

Representative true stress-true strain curves are shown in Figure 9 for b1, b12, b20 and b30 for both build directions. From these curves several trends are observed:

1. Ductility is lost as the powder is reused.

2. Plastic deformation after UTS decreases with powder reuse.

3. Strength increases with powder reuse.

4. Horizontal specimens are less ductile than vertical specimens.

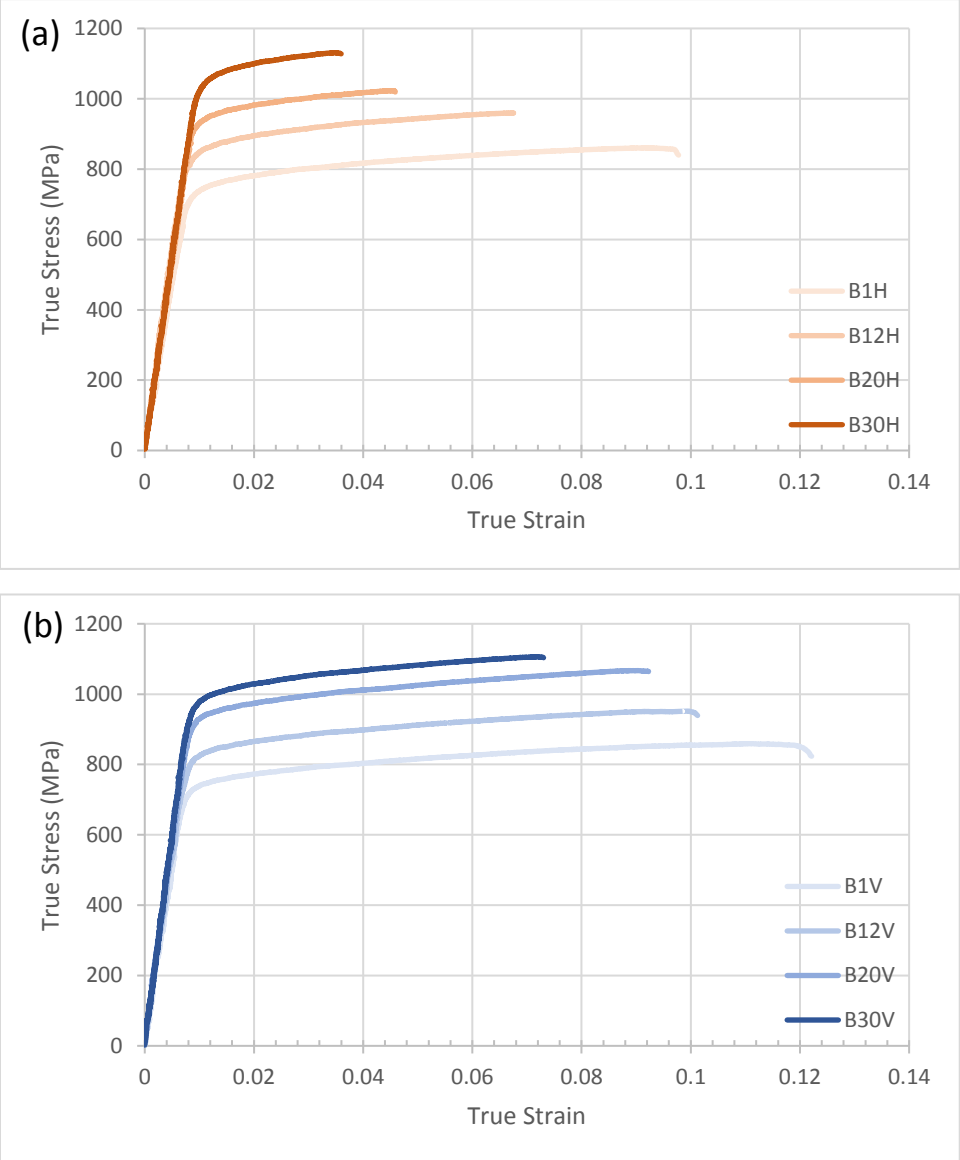

Figure 9: Representative true stress-true strain curves from b1, b12, b20 and b30 for the horizontal build direction (a) and vertical build direction (b).

To quantitively assess these trends, the modulus of elasticity, yield strength, ultimate tensile strength, % elongation, strain hardening exponent, and strength coefficient were calculated for each tensile specimen. These results were averaged according to specimen build direction (vertical or horizontal). The mechanical properties were determined through the build history and are plotted against the build number in Figure 10.

Figure 10 –

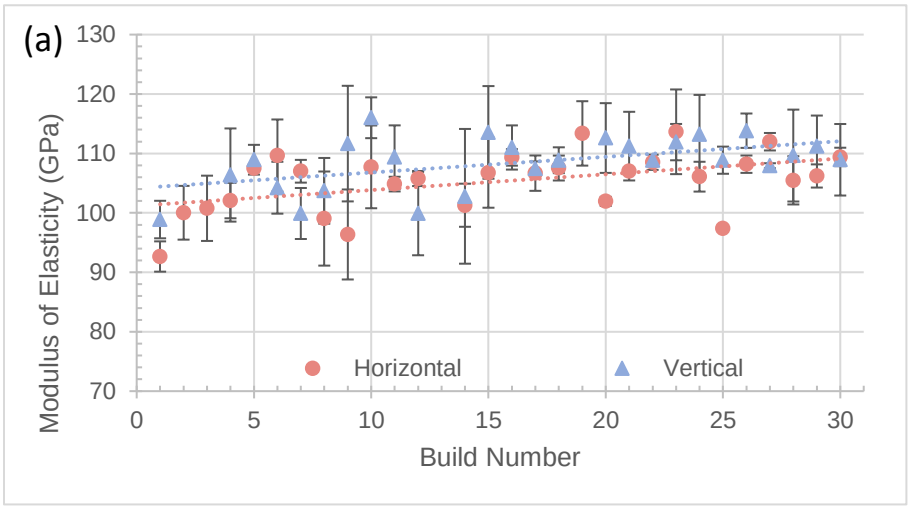
(a)
Modulus of Elasticity (GPa)
130
120
110
100
90
80
70
0
5
10
15
20
25
30
Build Number
Horizontal
Vertical

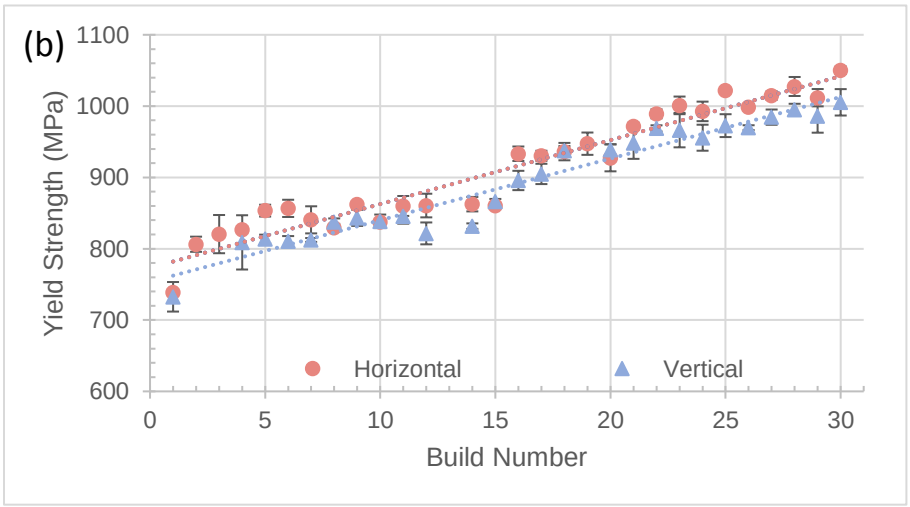
(b)
Yield Strength (MPa)
1100
1000
900
800
700
600
0
5
10
15
20
25
30
Build Number
Horizontal
Vertical

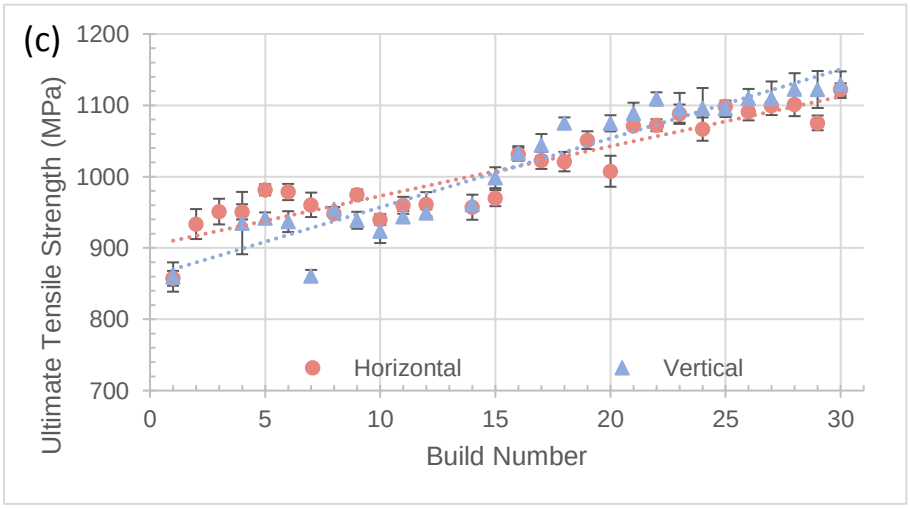
(c)
Ultimate Tensile Strength (MPa)
1200
1100
1000
900
800
700
0
5
10
15
20
25
30
Build Number
Horizontal
Vertical

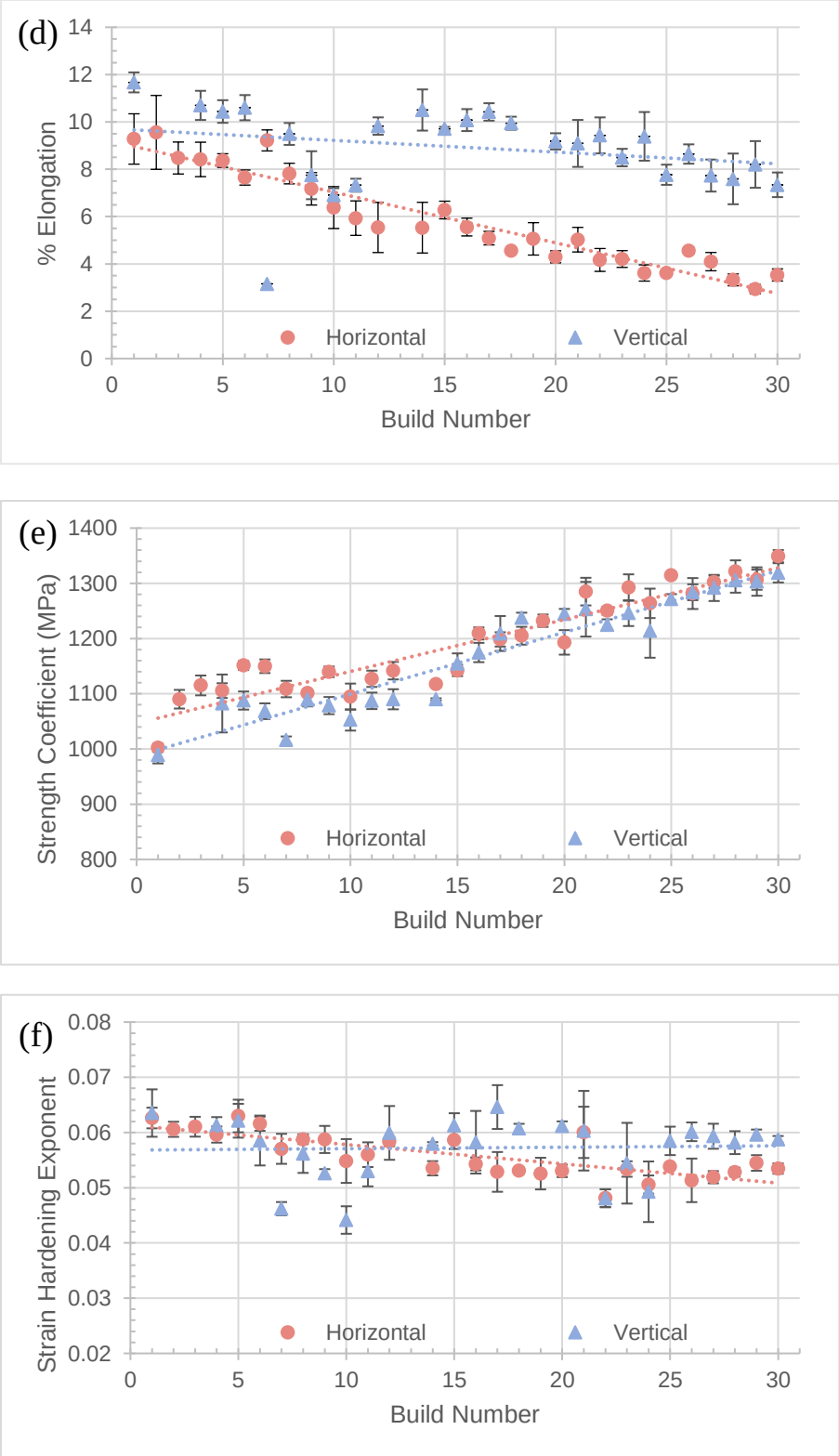

Figure 10: Plots of the modulus of elasticity (a), yield strength (b), ultimate tensile strength (c), % elongation (d), strength coefficient (e), and strain hardening exponent (f) versus build number.

The trends observed for each mechanical property are described below.

Elastic Modulus

The elastic modulus started at values of 98.9 and 100.6 GPa for the horizontal and vertical build directions respectively. As the powder was reused, there was a gradual increase in the elastic modulus for both build directions. The rate of increase was approximately equivalent for the build directions, at 0.43 and 0.44 GPa/build for horizontal and vertical build directions. By b30, the elastic modulus had increased to 109.4 and 108.9 GPa for the horizontal and vertical specimens. The vertical specimens were 2.8% higher than the vertical specimens on average.

Yield Strength

The yield strength began at 739 and 733 MPa for the horizontal and vertical directions respectively. The yield strength increased consistently for both build directions with build number. The horizontal specimens increased by approximately 7.8 MPa/build while the vertical increased by 8.8 MPa/build. At b30 the horizontal and vertical specimens reached yield strengths of 1050 and 1005 MPa. The horizontal specimens consistently exhibited higher yield strength than the vertical specimens, 2.4% higher on average.

Ultimate Tensile Strength (UTS)

The horizontal and vertical specimens began with UTS's of 888 and 859 MPa. The UTS increased as the powder was reused, 5.6 and 10.3 MPa/build for the horizontal and vertical directions, respectively. This large difference in the rate of strengthening resulted in the vertical

specimens closing the strength gap with the horizontal samples. By b30, the horizontal and vertical specimens reached 1122 and 1129 MPa.

% Elongation

The horizontal and vertical specimens began with 11.7 and 12.2 % elongation, respectively. The % elongation of the specimens decreased substantially over the 30 builds, losing approximately 0.27 and 0.05 % EL/build for horizontal and vertical specimens. This resulted in % elongations of 3.5% and 7.3% at b30. The vertical specimens displayed larger % elongation for every build except b7. The vertical specimens of b8-b11 also showed % elongation lower than expected based on the trend, however they remained higher than their respective horizontal specimens. There was a large standard deviation for most builds, averaging 0.54 % elongation.

Strength Coefficient

The strength coefficient of the horizontal and vertical specimens began at 1002 and 989 MPa. Both horizontal and vertical directions experienced a large increase in strength coefficient with build number, gaining 7.2 and 11.9 MPa/build respectively. While the horizontal specimens started with a slightly higher strength coefficient, the two strength coefficients converged by b15. The strength coefficient of the horizontal specimens was 2.3% higher than the vertical specimens on average.

Strain Hardening Exponent

The strain hardening exponent started at 0.063 and 0.064 for the horizontal and vertical directions. While the property changed from build to build, it trended to being nearly constant. The horizontal specimens decreased by -0.0005/build while the vertical increased by 0.0002/build.

2.3.3 Fractography

The fracture surfaces of the tensile specimens were analyzed using a stereomicroscope and SEM. Common macroscopic and microscopic features and trends are considered below.

Macroscopic

The tensile specimens showed little macroscopic deformation. There was a small degree of necking, shown in Figure 11. The amount of necking decreased with powder reuse, which can be seen by the decrease in plastic deformation after the UTS on stress-strain curves (Figure 9).

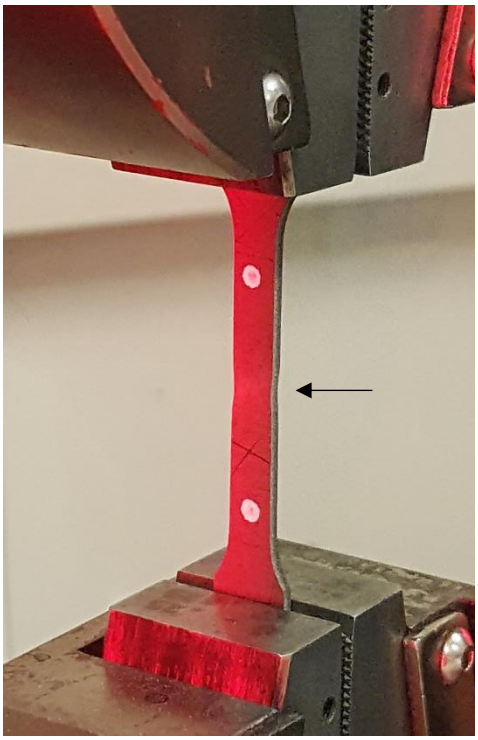

Figure 11: Neck forming during tensile testing.

The fracture surfaces often exhibit shear lips, with either single or double slant fractures. Examples of each are shown in Figure 12. These are ductile fracture features. With heavy powder reuse, the fracture surfaces of the horizontal and vertical specimens became flatter with a smaller shear lip region.

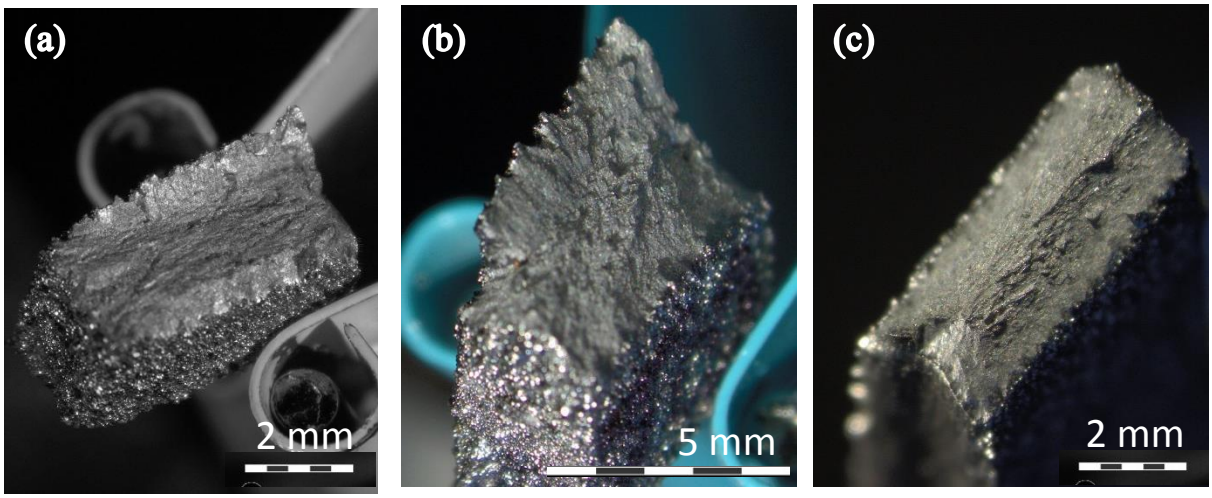

Figure 12: Examples of shear lips (a), single slant (b) and double slant (c) fractures.

Microscopic

The predominant feature on the fracture surfaces was micro-void coalescence, shown in Figure 13. This feature is an indicator of material ductility. Micro-void coalescence covers the majority of the fracture surface of the specimens, regardless of build number. In b20 onward, small localized regions of cleavage fracture appeared (Figure 14). This brittle fracture feature appeared predominately in horizontal specimens.

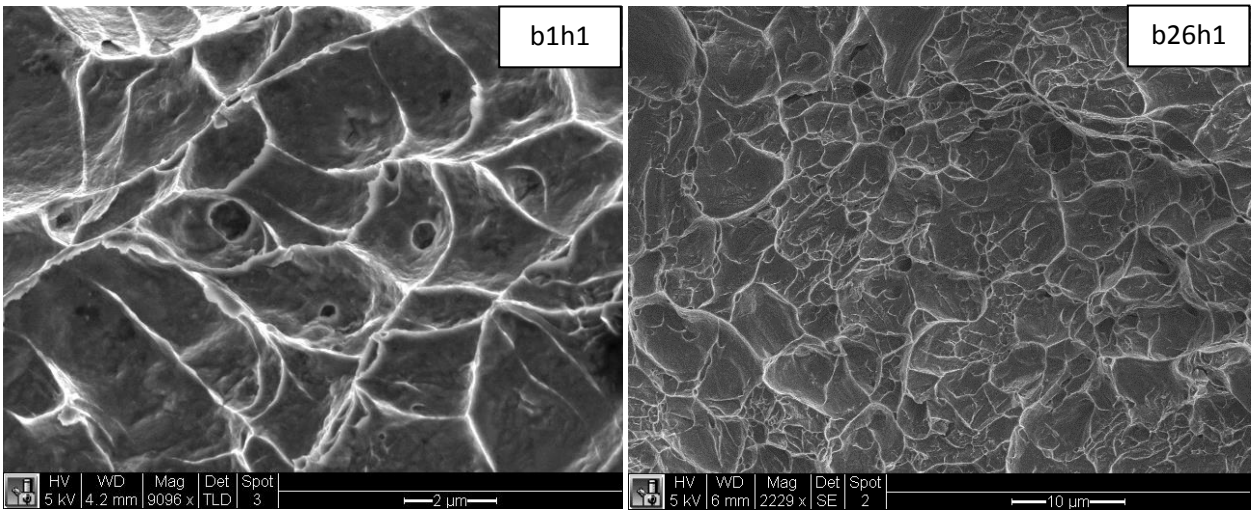

Figure 13: Micro-void coalescence seen on b1h1 and b26h1.

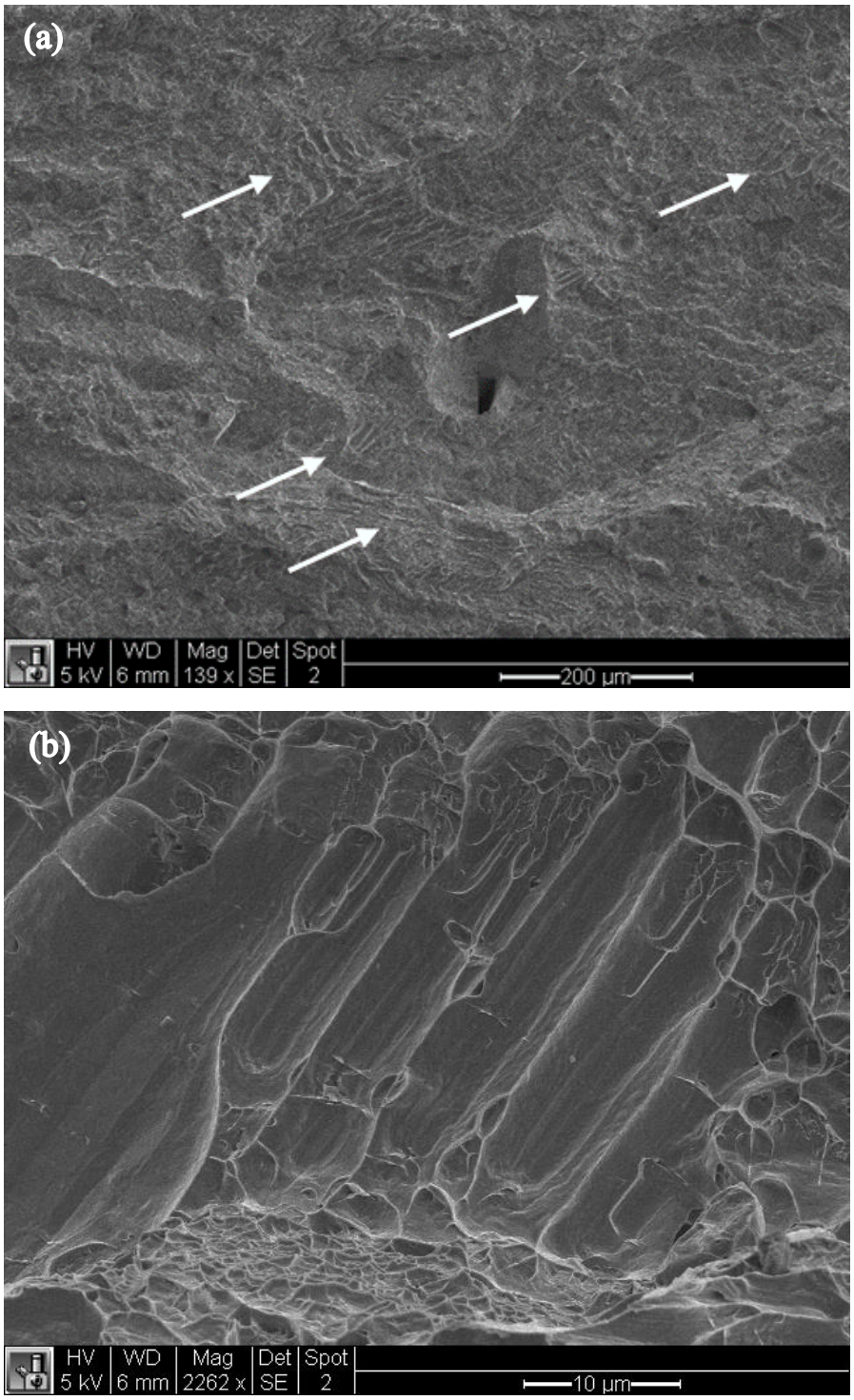

Figure 14: Cleavage planes from b26h1 indicated by arrows at low magnification (a) and high magnification (b).

Defects

Most of the specimens contained minor and major defects. A common minor defect are small, roughly spherical voids ranging from 20 μm to 50 μm in diameter. Two of these voids are shown in Figure 15 from b8v1. All of the specimens analyzed contained these small voids.

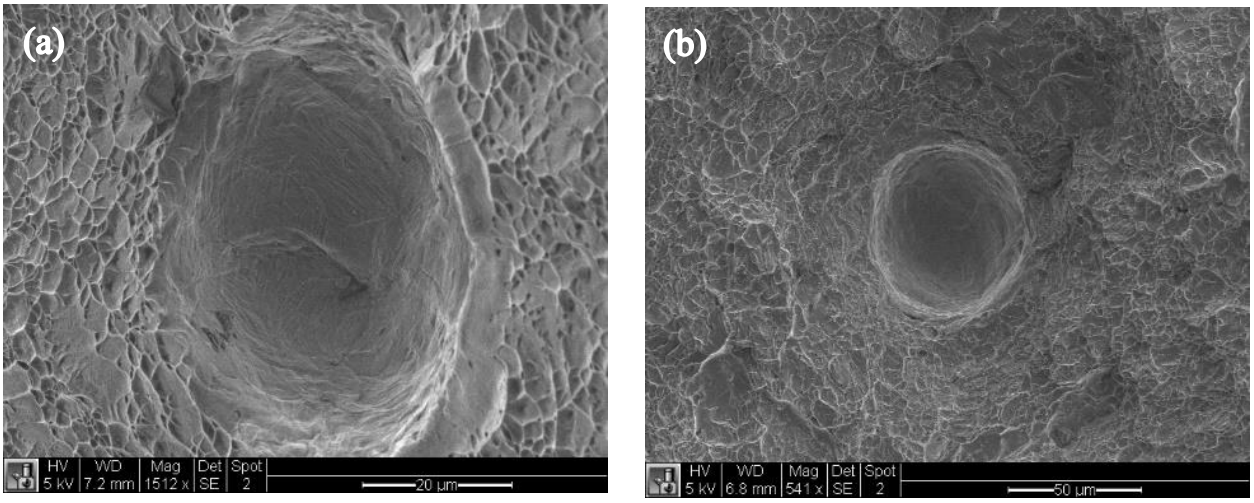

Figure 15: Spherical voids seen in b8v1.

Many of the horizontal specimens also contained significantly larger voids. These voids had a large aspect ratio, forming parallel to the build layers. Voids analyzed had widths as large as 970 μm and as tall as 200 μm. Most of the voids were considerably smaller, ranging from 100-200 μm in width and heights less than 50 μm. Examples of both sizes are shown in Figure 16. Many of these voids contained unmelted powder. Based on their orientation along build layers and size, these are likely lack of fusion (LOF) voids [7]. These voids form due to incomplete fusion of the build layer [8].

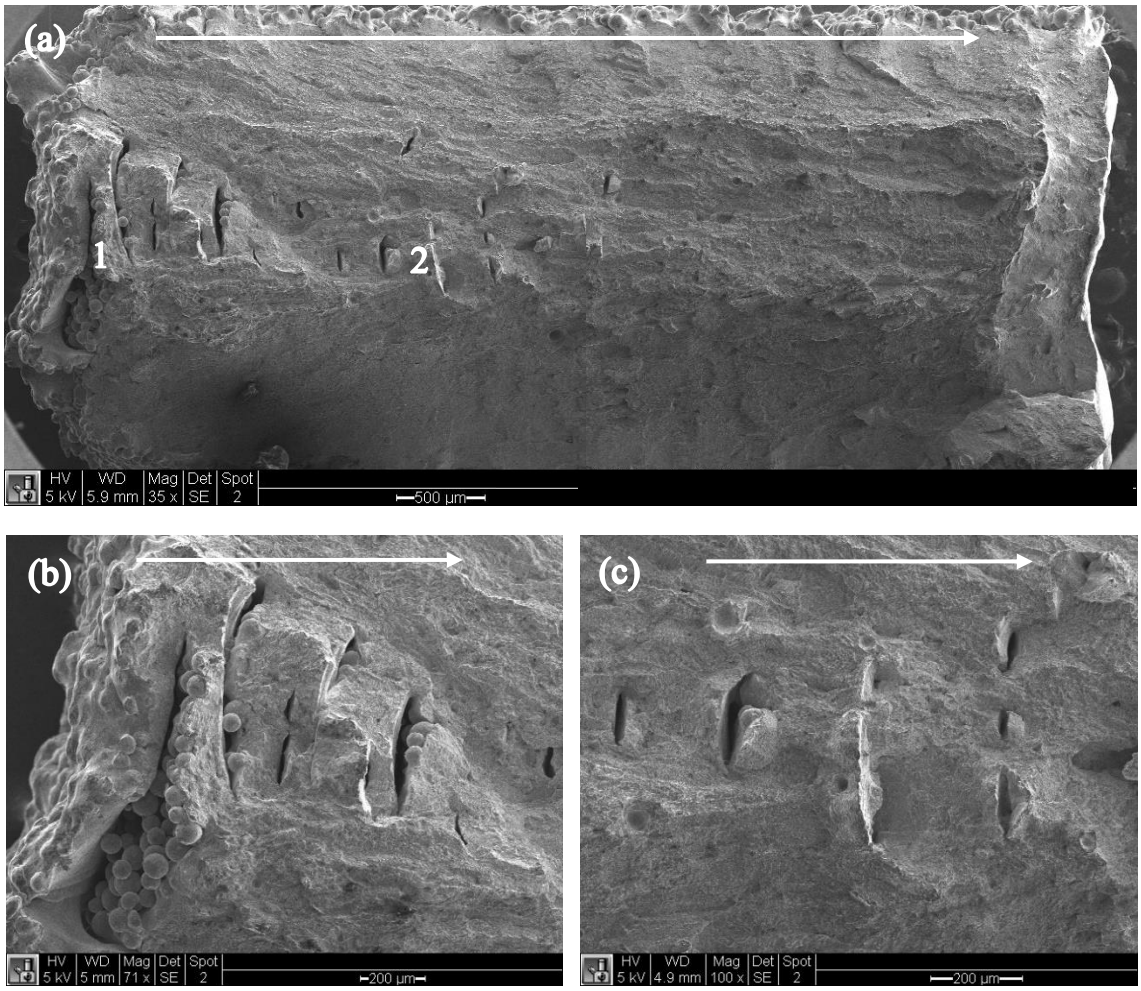

Figure 16: Macroscopic SEM image of b14h1 fracture surface (a) with enlarged areas showing LOF voids (b and c from locations 1 and 2 respectively). Build direction shown with arrows.

The vertical specimens of b7 showed particularly severe LOF voids. Large regions of sintered but unfused powder cover the fracture surface, seen in Figure 17a. Each particle of unfused powder has a small region of fracture surface on it. These are the remnants of sinter necks that attached these particles to adjacent particles or a fused region of the specimen, and subsequently broke during tensile testing. All the vertical specimens from b7 showed similar levels of unfused powder.

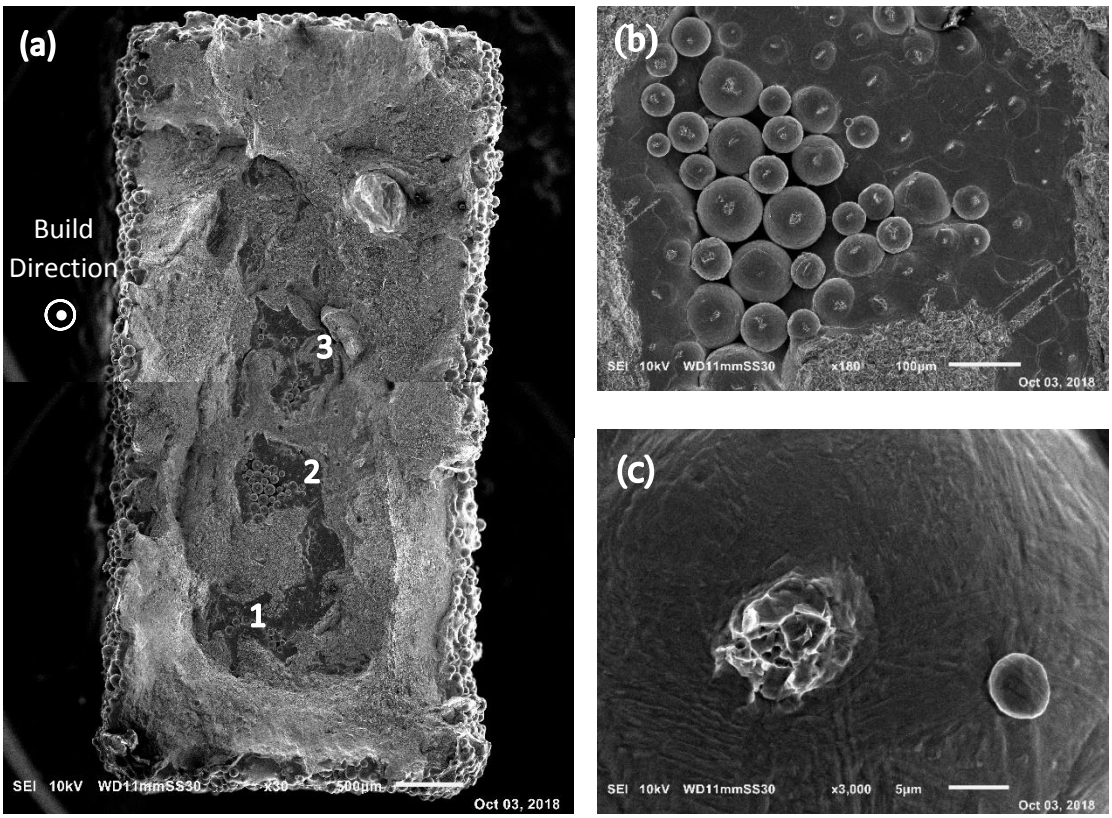

Figure 17: Macroscopic SEM image of b7v1fracture surface with regions of unmelted powder labelled 1-3 (a), sintered powder present at location 2 (b) and a closeup of a sinter neck on a particle (c).

There are also regions of partially fused powder seen in Figure 17b. This feature was also seen in small, localized regions in b8v1 and b30v1. These features are magnified in Figure 18.

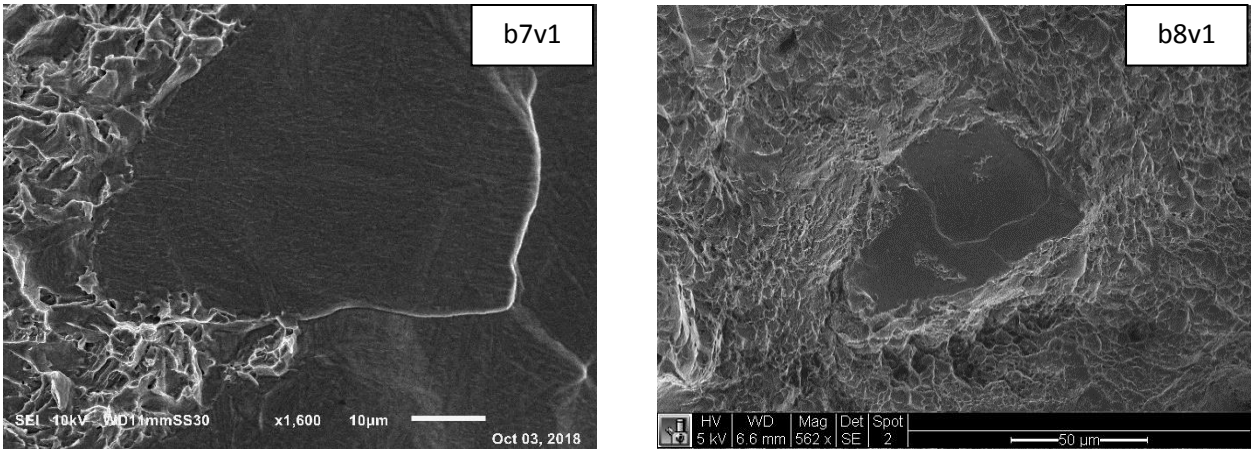

Figure 18: Regions of partially fused powder seen on b7v1 and b8v1.

The vertical and horizontal specimens also contained patches of smooth fracture surface, seen in Figure 19. These vary in size and aspect ratio.

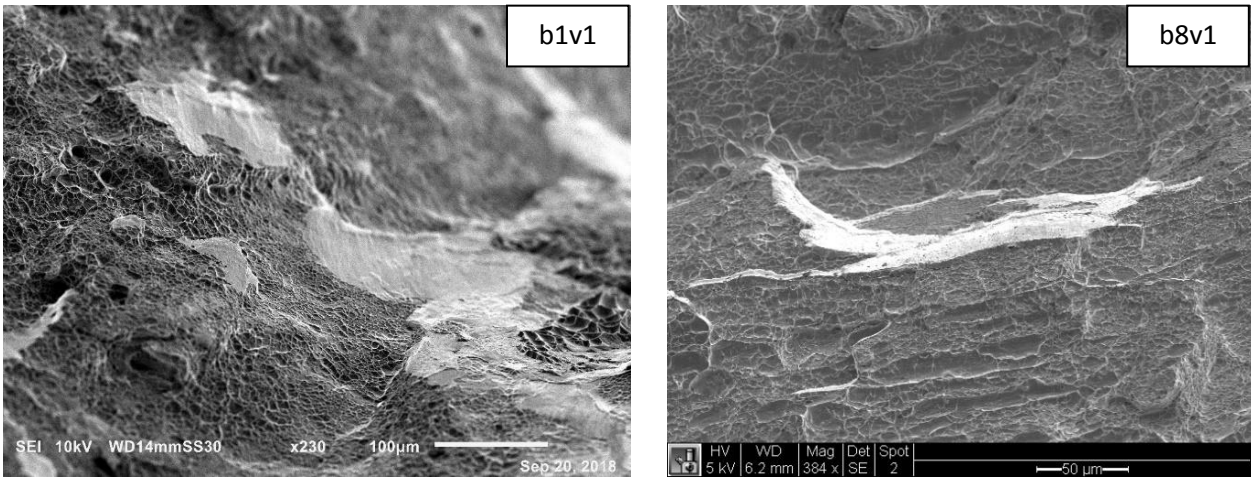

Figure 19: Smooth patches on the fracture surfaces of b1v1 and b8h1.

Another common feature are cracks. Cracks are found on both horizontal and vertical specimens. These are differentiated from voids by the presence of void coalescence inside the crack, indicating these surfaces were previously fused together. They could have formed during cooling

or tensile testing. An image of a crack and the interior surface are shown in Figure 21. Cracks seen range in size from 10-200 μm and are primarily interior cracks. One particularly large crack was seen in b26h1. Images of the crack are shown in Figure 20.

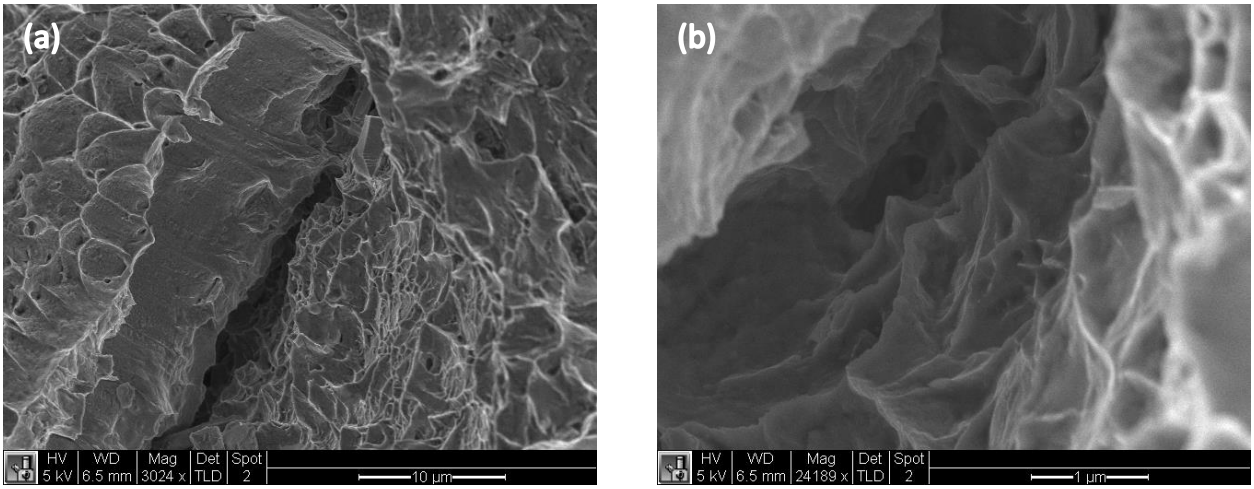

Figure 21: SEM image of a crack from b8v1 (a) and its interior (b).

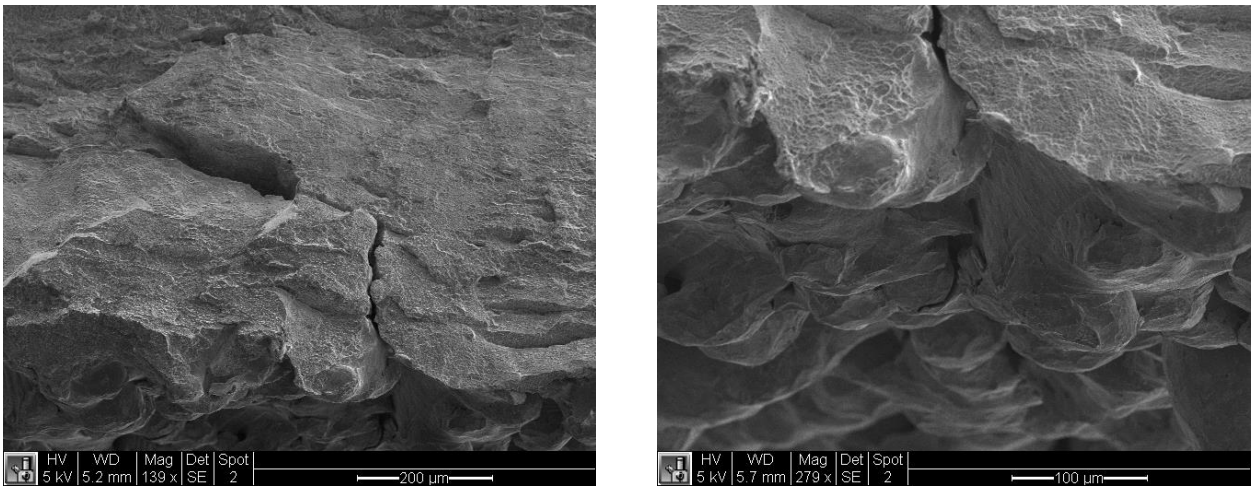

Figure 20: Large surface crack seen in b26h1.

Inclusions were found in many of the samples. Examples of these inclusions are shown in Figure 22. In this case, the inclusions were primarily deposited along a single build layer. EDS analysis of the inclusions revealed that they were mostly composed of Ti and O. Other specimens had inclusions that were more evenly dispersed through build layers.

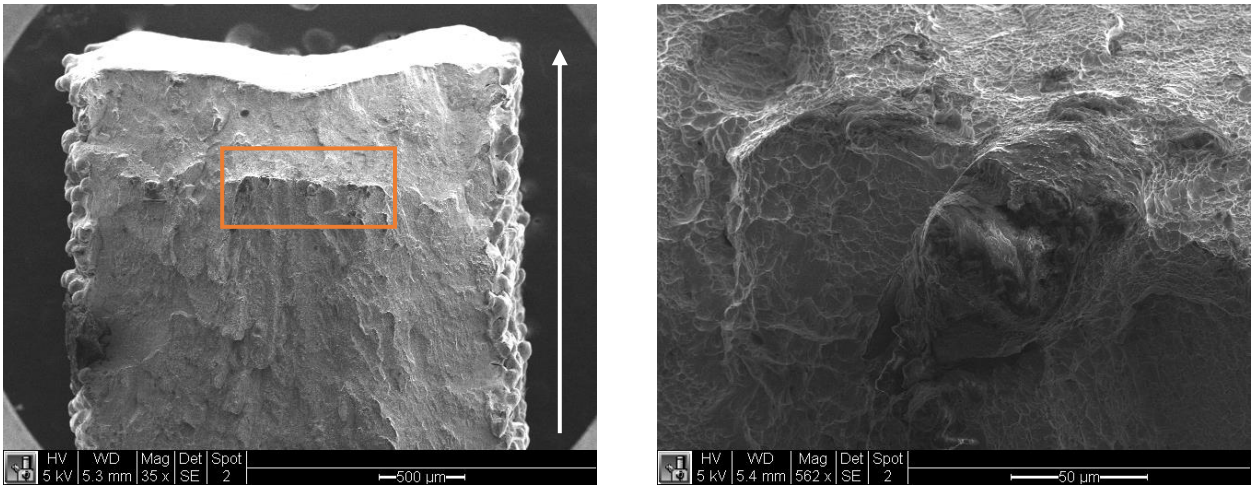

Figure 22: Inclusions seen in b7h1. Build direction is noted with an arrow.

Fracture Origins

The origin of fracture was at major defects for most specimens, especially LOF voids and inclusions. Examples of these cases are shown in Figure 23, with arrows indicating the fracture origin.

The horizontal specimens preferentially failed near the top (melt pool surface) of the specimens. Failure at this location, illustrated in Figure 24, was clear for 9 out of the 11 samples analyzed.

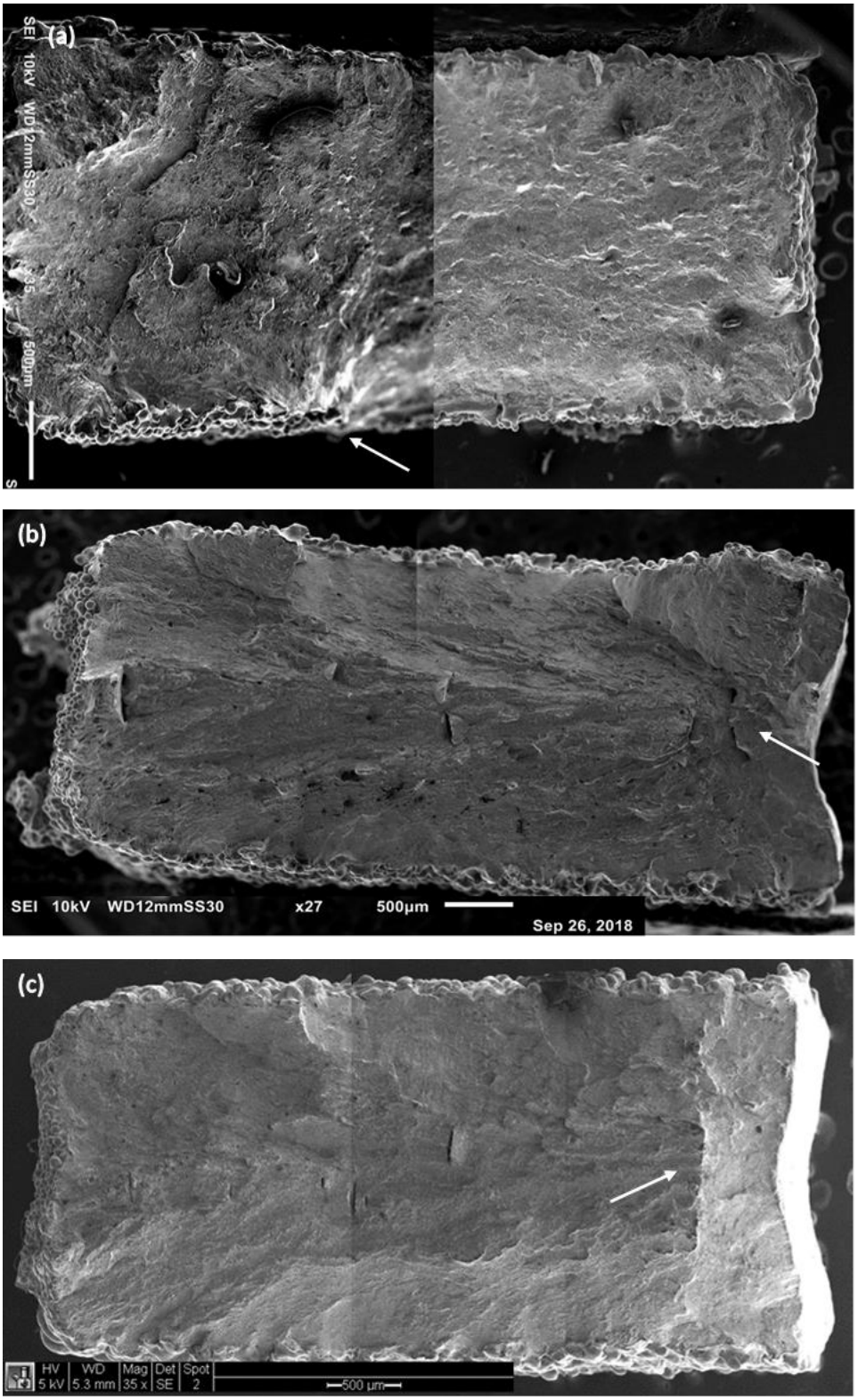

Figure 23: Fractures originating at LOF voids in vertical (a) and horizontal specimens (b), and at inclusions (c).

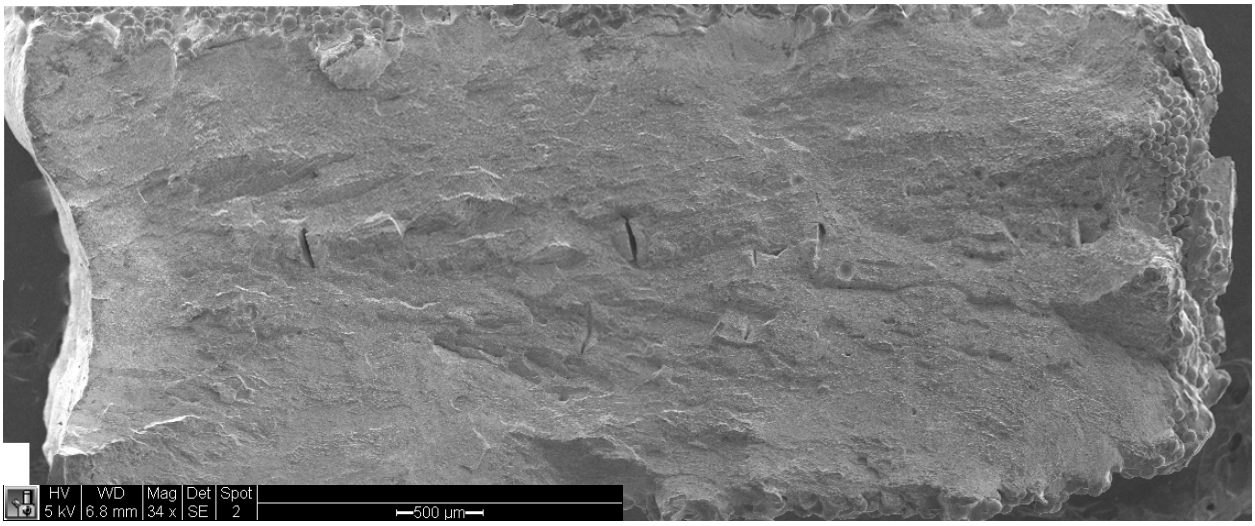

Figure 24: Horizontal specimen with the origin of fracture at the melt pool (left side).

2.4 Discussion

2.4.1 Profilometry

The roughness on the vertically oriented surfaces (all measured surfaces except the melt pool) using virgin powder ranged between 27-37 µm. This is slightly higher than the 25 µm Arcam claims is possible, but falls in line with literature [9],[10]. The large surface roughness is due to the presence of partially fused powder particles on the exterior of the parts. Various factors such as particle size distribution, beam energy and beam speed can all affect the fusion of powder particles to the surface of the parts [11].

The melt pool surface had a significantly lower Ra of 7.4 µm, well below Arcam's expected value of 35 µm. Since each layer is allowed to solidify before new powder is raked over the top,

horizontal free surfaces (excluding overhangs) will not have powder bonded to them. This can be seen visually in Figure 5, and results in a low Ra of the melt pool.

A similar relationship between the vertically oriented surfaces and the melt pool was seen for the ten point height (Rz). The vertically oriented surfaces for b1 had Rz values from 112-127 μm, while the melt pool Rz was only 13 μm. This large difference is again due to the presence of unmelted powder coating the vertically oriented surfaces and absence on the melt pool. 94% of the powder falls between 45-106 μm, leading to Ra and Rz values on the same scale (Arcam powder analysis, Appendix A).

There is a small decrease in Ra and Rz with build number for the vertically oriented surfaces. This is likely due to the narrowing particle size distribution seen in Appendix E. The largest and smallest particles are converging on a median value. Since the roughness of these surfaces is due to unmelted powder particles, a decrease in particle size would lower the roughness. The melt pool surface showed no change with build number.

2.4.2 Fractography

The specimens contain a large number of defects which can be seen on the fracture surfaces. One such defect are the many small, circular voids. These voids could originate from gas trapped within the powder from the gas atomization process, the presence of which was confirmed by Svensson et al. [12]. Due to their small size and circular shape, they likely play a minor role in decreasing the strength of the material.

Of more concern to the mechanical properties are the large, elongated LOF voids seen in the horizontal specimens (Figure 16). These are found in nearly all of the horizontal specimens, ranging from 2-12 voids per fracture surface.

If LOF voids are present in vertical specimens, they would take on a different appearance in fracture surfaces than in horizontal specimens. This is because the build layers, and therefore any LOF voids, are in plane with the vertical specimen's fracture surface. This would reveal the interior of LOF voids instead of a cross section as seen in the horizontal specimen fracture surfaces. Most vertical and some horizontal specimens contained areas of smooth fracture surface, seen in Figure 19. Due to their orientation being predominantly along build layers and their smooth texture, these surfaces were hypothesized to be the interior surface of lack of fusion voids.

To investigate this theory, lack of fusion voids from b2 and b14 horizontal specimens were found and the interior surfaces were imaged. The locations of these LOF voids on the fracture surfaces are shown in Figure 25. The interior surfaces of these voids were then compared with the suspected LOF voids.

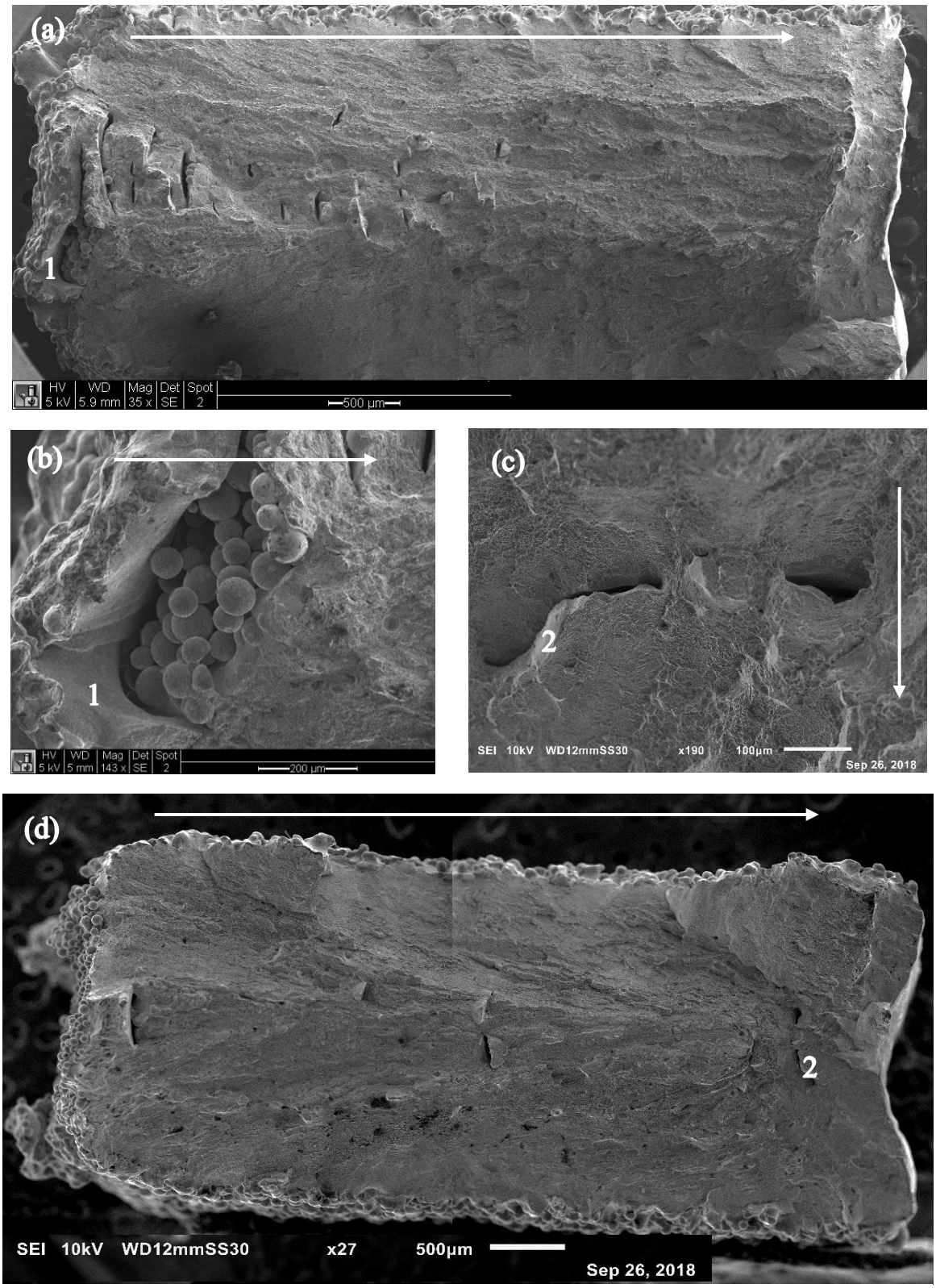

Figure 25: LOF voids at low magnification (a and d) and higher magnification (b and c). The location of the voids is denoted on the low and high magnification images with matching numbers. The build direction is shown on each image with an arrow.

Figure 26 shows similarities at both low magnification (a and b) and high magnification (c and d). A parallel grooved pattern is visible at low and high magnification in both the suspected and confirmed LOF voids, suggesting that these surfaces are the interior surfaces of LOF voids. However, a few samples have a similar feature that appears to cross multiple build layers, casting doubt on this theory.

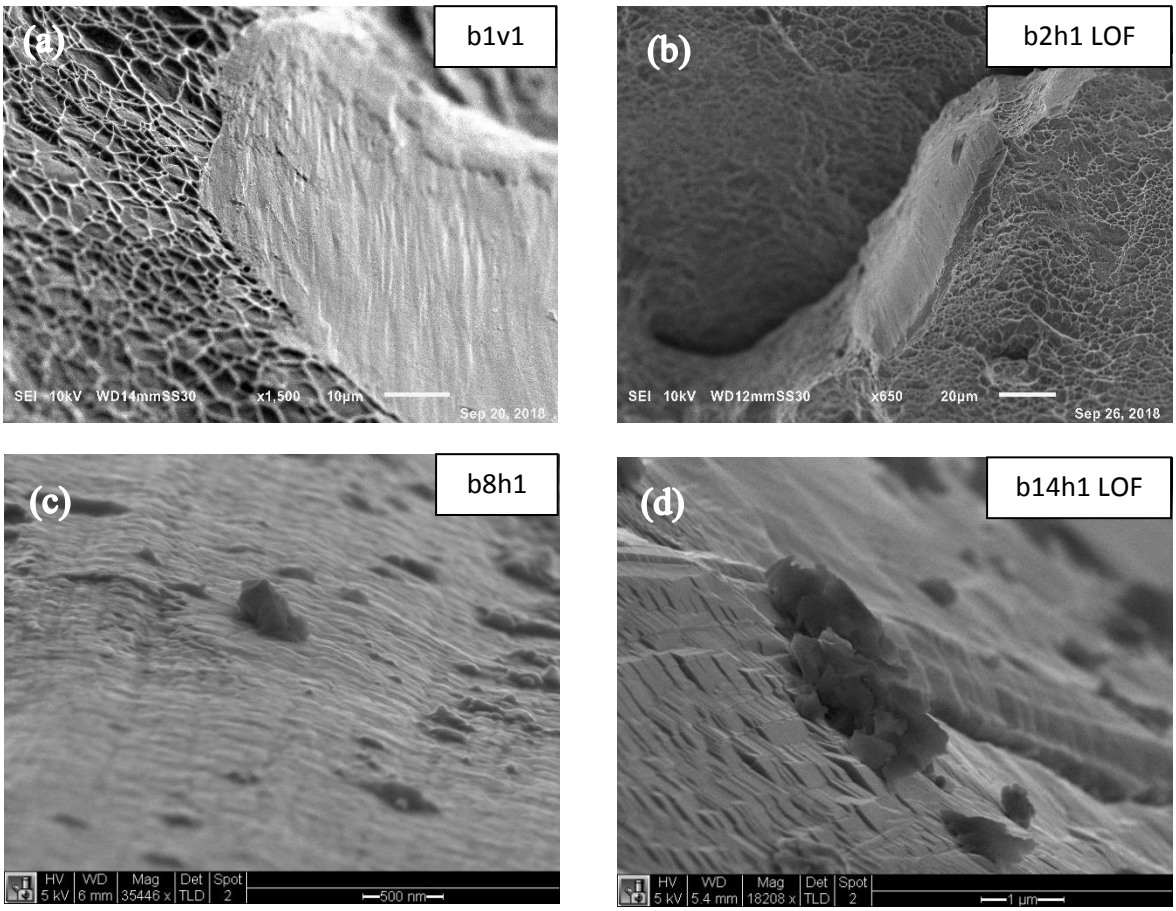

Figure 26: SEM images comparing suspected lack of fusion voids (a and c) with confirmed lack of fusion voids (b and d).

In the vertical specimens, LOF voids are in mode I loading during tensile testing, posing a much larger problem than for the horizontal specimens where they are closed by loading.

Failures typically originated at major defects such as LOF voids and titanium oxide inclusions. These large defects create stress concentrations that help to initiate failure. Furthermore, the horizontal specimens preferentially failed at the melt pool surface or at stress concentrators near the melt pool. This was true regardless of whether there were large voids elsewhere on the fracture surface. Coarsening of the microstructure with build height has been shown to reduce the % elongation for a horizontal loading direction, offering a possible explanation for the preferential failure near the top of these specimens [13].

On the macro and meso scale, the tensile specimens exhibit a transition from ductile features to brittle features with powder reuse. With virgin and lightly reused powder, the fractures are predominantly slant fractures and often contain shear lips, both of which are ductile features. There is also a small degree of necking. With heavy powder reuse, the fracture surface becomes flatter, the area consumed by shear lip decreases, and the degree of necking decreases. All of these signs indicate decreasing ductility.

On the microscopic scale, the specimens display a similar transition from ductile to brittle features. Micro-void coalescence is the main feature on this scale, covering the majority of the fracture surfaces. In later builds, small regions of cleavage planes appear, especially on the horizontal specimens. This indicates a loss of ductility on the material level.

2.4.3 Tensile Testing

Virgin Powder

The b1 elastic modulus, yield strength, UTS and % elongation are shown in Table 2. The minimum values required by ASTM for additively manufactured Ti-6Al-4V and the properties Arcam claims are possible with virgin powder are also shown for comparison [3]. All four properties fell below Arcam's expected values. Furthermore, the elastic modulus, yield strength, and horizontal specimen % elongation were below ASTM requirements for AM material. The UTS and vertical specimen % elongation met the ASTM requirements.

Table 2 Comparison of measured mechanical properties using virgin powder with Arcam's quoted values and ASTM standards.

	Elastic Modulus (Gpa)	Yield Strength (MPa)	UTS (MPa)	% Elongation
b1h avg	93	739	857	9.3
b1v avg	101	761	888	11.7
Arcam	120	950	1020	14
ASTM AM	120	825	895	10

While the low properties could be due in part to processing parameters, another possibility is that irregular geometry of the tensile coupons affected the cross-sectional area measurements, and by extension the elastic modulus, yield strength, and UTS. Geometric deviations are especially apparent on the horizontal specimens. These specimens contain two large deviations from ideal geometry: the concave melt pool and the irregular surface where support structures were removed. These irregularities are apparent in Figure 27. Since the specimen dimensions were measured in the as-built condition, these deviations in geometry were carried through into cross-sectional area measurements. The nature of these geometric variations results in an

overestimation of the cross-sectional area, and an underestimate of the elastic modulus, yield strength, and UTS. The large surface roughness present on the specimens would also inflate the measured cross-sectional area for both vertical and horizontal specimens.

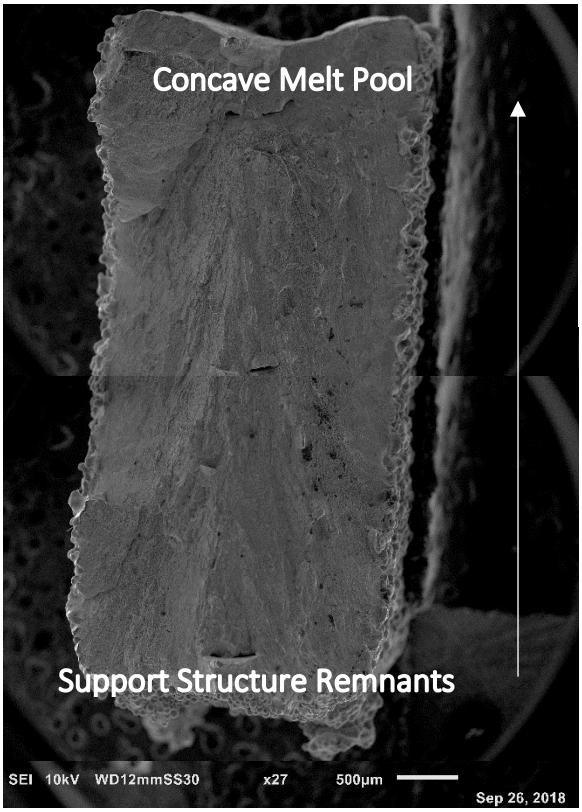

Figure 27: Cross section of a horizontal tensile specimen showing geometry irregularities and surface roughness. Build direction shown with an arrow.

To assess the impact of irregular geometry on the calculated properties, the gauge sections of a vertical and horizontal specimen from b4 (v2 and h2) were lightly sanded to produce a finish free of large irregularities. Table 3 compares the properties of sanded and as-built specimens and includes the % increase in properties after sanding.

Table 3: Comparison of as-built and polished samples.

	Elastic Modulus (Gpa)	Yield Strength (MPa)	UTS (MPa)	% Elongation
b4 horizontal as-built	102	827	951	8.4
b4 horizontal sanded	117	928	1057	9.7
% increase	14.7	12.2	11.1	15.5
b4 vertical as-built	106	809	935	10.7
b4 vertical sanded	117	880	987	11.2
% increase	10.4	8.8	5.6	4.7

From Table 3 it is apparent that geometric deviations and surface roughness play a large role in the measured elastic modulus, yield strength, UTS and % elongation. The bigger change in properties of the horizontal specimens is likely due to the size of the geometric irregularities of the melt pool and support structures, which are not present on the vertical specimens. The vertical specimens still showed increases in properties of 4.7%-10.4% after the removal of the surface roughness. While the sanding process could have introduced residual stresses that artificially affected the material's strength, the large change in elastic modulus, a property not impacted by residual stress, suggests that the geometric change is the primary factor creating the increase in properties.

Unlike the elastic modulus, yield strength and UTS, the % elongation does not depend on cross-sectional area measurements. Regardless, it increased significantly after the sanding treatment for both build directions. This indicates that the surface roughness or exterior layers of solid material play a large role in the failure of these samples.

Other groups have also reported that polishing significantly improves mechanical properties [14]. Formanoir et al. determined that approximately 150 μm on each surface is not load bearing due to the surface roughness, equating to an increase of the elastic modulus and yield strength by 23% for their specimens [14]. This depth of 150 μm matches well with our measured Rz value of 112-127 μm for b1, suggesting that Rz might be used as a correction to estimate the true material properties.

To get a rough idea of the true mechanical properties of the b1 virgin material, the % change in b4 properties after sanding is applied to the b1 data, shown in Table 4. Using this correction, the mechanical properties excluding elastic modulus now exceed the minimum properties required by ASTM for AM parts, but still fall below what Arcam claims is possible.

Table 4: Comparison of mechanical properties of virgin powder corrected for geometry irregularities with Arcam's quoted values.

	Elastic Modulus (Gpa)	Yield Strength (MPa)	UTS (MPa)	% Elongation
Corrected b1 horizontal	106	829	953	10.7
Corrected b1 vertical	111	828	938	12.2
Arcam	120	950	1020	14
ASTM AM	120	825	895	10

Horizontal vs. Vertical Orientations

Several of the mechanical properties showed clear differences between the horizontal and vertical build directions. The elastic modulus, yield strength and strength coefficient all showed

between 2-3% difference between the build directions. These properties are intrinsic to the material and are only dependent on the chemistry and microstructure. The chemistry of all parts within a batch should be similar, suggesting that the difference in properties is due to the microstructure. This is plausible given that AM produces a directional microstructure comprised of columnar β grains with a basketweave structure in between. Hayes et al. hypothesizes that this structure can lead to a 3% difference in strength between build directions, closely matching our results [15].

The % elongation was also build direction dependent. The horizontal specimens consistently had lower % elongation than the vertical specimens. One possible explanation is the oriented microstructure. The vertically oriented prior β grains might impede dislocation motion when loading is perpendicular to the grains, causing a buildup of damage and premature failure not seen when loading is parallel to the prior β grains. β grains within Ti-6Al-4V α/β lamellar structures have been shown not to impede dislocations within the lamellar colonies; however an orientation mismatch between prior β grains and lamellar colonies might be sufficient to stop dislocation motion [16]. Electron backscatter diffraction of AM Ti-6Al-4V has been used to show that there is a large grain orientation mismatch of 60-90^{o} across prior β grains [17]. Another explanation put forward by Tan et al. to explain the high elongation of vertically oriented specimens is that of a graded microstructure [13]. The observed microstructure begins with equiaxed grains, transitions several build layers up to closely spaced prior β grains with α/β basketweave colonies in between, and coarsens with further build height. They believe this structure allows for large deformation due to the distribution of plastic deformation among the

gradient in grain sizes [13]. Further analysis is needed to determine the root cause of the anisotropy in % elongation.

Trends with Powder Reuse

All the mechanical properties showed large changes with powder reuse except the strain hardening exponent. The strain hardening exponent was not significantly affected by the reuse. Yield strength, ultimate tensile strength, and strength coefficient increased significantly with build number. There are several possible explanations for this trend. One likely cause is oxidation. Titanium has a high affinity for oxygen, and it is well known that oxygen interstitials strengthen the alloy [18]. While the printing itself is done under vacuum, there are opportunities for oxidation of the powder to occur during powder handling. Complimentary work within the lab shows a consistent increase in oxygen content of the powder with build number, see Appendix D for figures. By b11 the oxygen content reached 0.2 wt%, exceeding the limit imposed by ASTM F2924 for Grade 5 Ti-6Al-4V [3]. In a similar study using ELI Ti-6Al-4V, Tang et al. found that over 21 powder reuses, oxygen content in printed parts increased from 0.07 wt% to 0.18 wt% [19]. They further showed that the oxygen content of a printed part was comparable to that of the powder used to create it.

Deviations in microstructure could also result in an increase in strength. It is generally assumed that EBM based AM produces columnar β grains with Widmanstätten (basketweave) colonies due to the cooling rate, however a change in the size of the basketweave, the presence of equiaxed grains, or a transition to α’ martensite could change the strength [13],[14].

Complimentary microstructure analysis within the lab showed only minor changes in the size of α laths and prior beta width with build number, see Appendix F for plots. There was no α' martensite seen in the specimens. Furthermore, while changes in microstructure do affect the strength, Hayes et al. showed that solid solution strengthening plays the dominant role in strengthening [15]. When taken together, this information suggests that oxidation is the primary factor in strengthening the material.

The elastic modulus also increased with build number, but at a slower rate. This change, like the strengthening, could be attributed to oxidation. As the wt% of oxygen increases, so too does the elastic modulus.

The largest change seen with powder reuse was in the ductility. The % elongations of the horizontal and vertical specimens decreased by 61.9% and 37.1% from b1 to b30. This large decrease could be a result of many factors; oxidation, microstructure, surface quality, and defect severity, type and quantity could all play a role in the ductility drop. Since there was a small decrease in Ra and Rz from b1 to b30 and micro-CT did not show a significant increase in the volume fraction of voids (Appendix G), it is likely that oxidation played the dominant role in the ductility drop. The oxide inclusions and brittle cleavage planes seen in the fracture surfaces made with heavily reused powder support this theory, along with the confirmed oxidation of the powder.

The horizontal specimens' % EL decreased by approximately 0.21% EL/build, while the vertical specimens' decreased by only 0.05% EL/build, roughly 4 times slower. This large divergence between the horizontal and vertical directions is not seen in the other mechanical properties. Since oxygen preferentially occupies α phase, it could result from the loading direction applied to the embrittled α phase, however further investigation is needed [13].

There were two deviations in the trends seen for the % elongation of the vertical specimens. The first is b7 where there was prolific lack of fusion across the build. While the log files from the machine show no anomalies or errors in the build, metallization falling onto the powder bed is a likely cause. The metallization would have been vaporized as the beam passed over it, leaving unmelted powder underneath. The second deviation was a large decrease in % elongation of vertical specimens for builds b9-b11. These builds were 19-26% lower than their neighboring builds. Fractography of b10v1 showed many patches of the smooth fracture surface believed to be LOF voids, shown in Figure 28. Metallization could again be the cause of this.

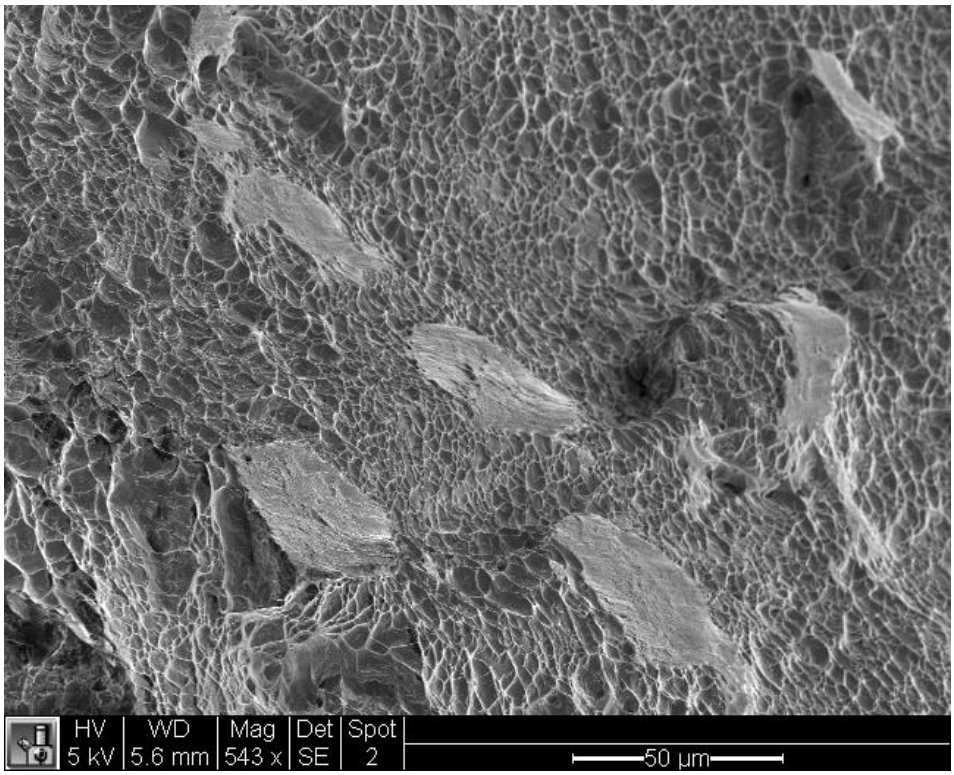

Figure 28: Smooth fracture features seen in b10v1.

3. Conclusions and Future Work

3.1 Conclusions

Several important trends were observed over the duration of this study. The first trend was the difference in properties between the horizontal and vertical build directions. Within the AM research community, there has not been a consensus on whether mechanical properties are isotropic or anisotropic; some groups found minor directional dependence, while others found no directional dependence at all [6,12]. Our results show that for most properties there is a small degree of anisotropy. The elastic modulus, yield strength, and strength coefficient showed a minor dependence on build direction, where the percent difference between horizontal and vertical directions was 2-3% across the build history. The UTS showed almost no orientation

dependence, with an average percent difference of 0.3%. The strain hardening exponent also showed minimal directional dependence, with just 1.7% difference between the horizontal and vertical directions. The % elongation showed a large dependence on build direction, however, with the horizontal specimens consistently lower in ductility than the vertical specimens.

The anisotropy seen can largely be explained by the grain structure of the specimens. The microstructure contains columnar prior β grains oriented parallel to the build direction with Widmenstätten structure filling the space in between. This structure leads to anisotropy in the mechanical properties. The larger orientation dependence of the % elongation could be due to microstructure as well; dislocation pinning by the prior β grains for the horizontal loading direction would be absent in the vertical direction, making the horizontal direction brittle.

This study also revealed that powder reuse has a major impact on the mechanical properties of EBM additively manufactured components. Significant changes were seen in the elastic modulus, yield strength, ultimate tensile strength, % elongation, and strength coefficient as the powder was reused. The only property that did not exhibit a large change was the strain hardening exponent. The % elongation decreased linearly with build number, while the other properties increased linearly. These trends can largely be explained by oxidation. Chemical analysis by other researchers in our lab showed a linear increase in oxygen content of the powder as it was reused. Oxygen interstitials are known to strengthen and embrittle titanium alloys, and the strengthening model put forward by Hayes et al. identifies solid solution strengthening as the dominant strengthening mechanism in AM Ti-6Al-4V [15]. Other factors such as microstructure

may be playing a smaller role. Future work from our lab will include tensile specimen microstructure analysis with build number, including prior β spacing and α lath thickness, and correlating any changes to the mechanical properties.

Fractography supported the conclusions made about the mechanical properties. As the powder was reused, fracture surface features changed from ductile (micro-void coalescence, slant fracture etc.) to brittle (flat fracture, cleavage planes). Furthermore, analysis of the horizontal specimens revealed that fracture primarily originates at or near the melt pool.

The results of this study can help guide decisions made regarding powder reuse and part design for the AM build space. Knowledge of how mechanical properties evolve with powder reuse empowers manufacturers to shape powder reuse practices to achieve desired properties or prevent properties from falling below critical thresholds, all while reducing material waste. An understanding of anisotropy in mechanical properties allows engineers to orient parts within the build chamber to fully utilize the strengths of the material. Finally, knowing where failures originate in AM parts allows engineers to design parts around these problem areas to prevent early failures.

3.2 Future Work

The work presented here is part of an ongoing study. Those involved will continue to look at the effects of Ti-6Al-4V powder reuse on AM parts. The second phase of this study will utilize the banked tensile specimens from each build (h2, h4, h6, v2, v4, v6) to analyze post processing of

AM parts made with reused powder. Two post processing techniques, heat treatment and machining, will be analyzed. The heat treatment will be utilized to boost the ductility of the specimens, hopefully counteracting some of the effects of oxidation. Machining the specimens will reveal with greater certainty the effects of surface roughness on the failure of the specimens and cross-sectional area measurements, yielding the true mechanical properties of the material.

The results of this research also revealed several areas for future research, outlined below:

1. Alter contour beam parameters to minimize surface roughness.
2. Investigate why failure originates near the melt pool of horizontal specimens, starting with microstructure and micro hardness evaluations.
3. Determine the cause of anisotropy in ductility and why % elongation decreases 4X faster along the horizontal orientation.

Appendices

A. Powder Certification

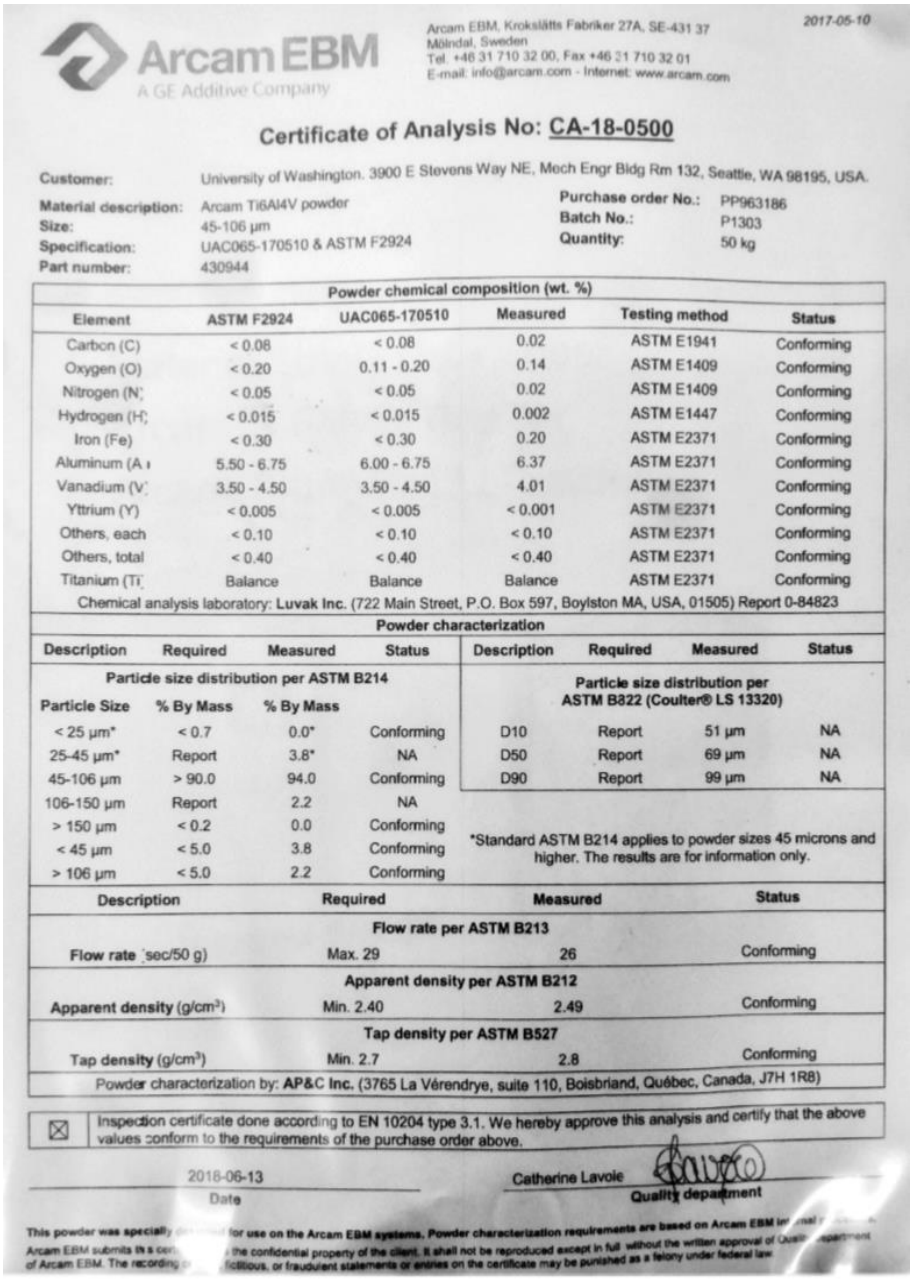

Arcam EBM
A GE Additive Company

Arcam EBM, Krokslätts Fabriker 27A, SE-431 37
Mölndal, Sweden
Tel. +46 31 710 32 00, Fax +46 31 710 32 01
E-mail: info@arcam.com - Internet: www.arcam.com

2017-05-10

Certificate of Analysis No: CA-18-0500

Customer: University of Washington. 3900 E Stevens Way NE, Mech Engr Bldg Rm 132, Seattle, WA 98195, USA.

Material description: Arcam Ti6Al4V powder
Size: 45-106 µm
Specification: UAC065-170510 & ASTM F2924
Part number: 430944

Purchase order No.: PP963186
Batch No.: P1303
Quantity: 50 kg

Powder chemical composition (wt. %)

Element	ASTM F2924	UAC065-170510	Measured	Testing method	Status
Carbon (C)	< 0.08	< 0.08	0.02	ASTM E1941	Conforming
Oxygen (O)	< 0.20	0.11 - 0.20	0.14	ASTM E1409	Conforming
Nitrogen (N)	< 0.05	< 0.05	0.02	ASTM E1409	Conforming
Hydrogen (H)	< 0.015	< 0.015	0.002	ASTM E1447	Conforming
Iron (Fe)	< 0.30	< 0.30	0.20	ASTM E2371	Conforming
Aluminum (Al)	5.50 - 6.75	6.00 - 6.75	6.37	ASTM E2371	Conforming
Vanadium (V)	3.50 - 4.50	3.50 - 4.50	4.01	ASTM E2371	Conforming
Yttrium (Y)	< 0.005	< 0.005	< 0.001	ASTM E2371	Conforming
Others, each	< 0.10	< 0.10	< 0.10	ASTM E2371	Conforming
Others, total	< 0.40	< 0.40	< 0.40	ASTM E2371	Conforming
Titanium (Ti)	Balance	Balance	Balance	ASTM E2371	Conforming

Chemical analysis laboratory: **Luvak Inc.** (722 Main Street, P.O. Box 597, Boylston MA, USA, 01505) Report 0-84823

Powder characterization

Description	Required	Measured	Status
Particle size distribution per ASTM B214			
Particle Size	**% By Mass**	**% By Mass**	
< 25 µm*	< 0.7	0.0*	Conforming
25-45 µm*	Report	3.8*	NA
45-106 µm	> 90.0	94.0	Conforming
106-150 µm	Report	2.2	NA
> 150 µm	< 0.2	0.0	Conforming
< 45 µm	< 5.0	3.8	Conforming
> 106 µm	< 5.0	2.2	Conforming

Description	Required	Measured	Status
Particle size distribution per ASTM B822 (Coulter® LS 13320)			
D10	Report	51 µm	NA
D50	Report	69 µm	NA
D90	Report	99 µm	NA

*Standard ASTM B214 applies to powder sizes 45 microns and higher. The results are for information only.

Description	Required	Measured	Status
Flow rate per ASTM B213			
Flow rate (sec/50 g)	Max. 29	26	Conforming
Apparent density per ASTM B212			
Apparent density (g/cm³)	Min. 2.40	2.49	Conforming
Tap density per ASTM B527			
Tap density (g/cm³)	Min. 2.7	2.8	Conforming

Powder characterization by: **AP&C Inc.** (3765 La Vérendrye, suite 110, Boisbriand, Québec, Canada, J7H 1R8)

☒ Inspection certificate done according to EN 10204 type 3.1. We hereby approve this analysis and certify that the above values conform to the requirements of the purchase order above.

2018-06-13
Date

Catherine Lavoie
Quality department

This powder was specially [illegible] for use on the Arcam EBM systems. Powder characterization requirements are based on Arcam EBM [illegible]. Arcam EBM submits its [illegible] the confidential property of the client. It shall not be reproduced except in full without the written approval of Quality Department of Arcam EBM. The recording [illegible] fictitious, or fraudulent statements or entries on the certificate may be punished as a felony under federal law.

B. Arcam A2X Printer and PRS

Melt Theme	
Beam Speed	4530 nm/s
Beam Current	15 mA
Max Current	20 mA
Focus Offset	25 mA
Speed Function	45
Snake	True
Line Order	1
Line Offset	0.2 mm
Randomized Hatch	False
Hatch Depth	0.05 mm
Speed Factor	1.5 mm
Thickness Factor	0 mm

Processing parameters used for the duration of the study.

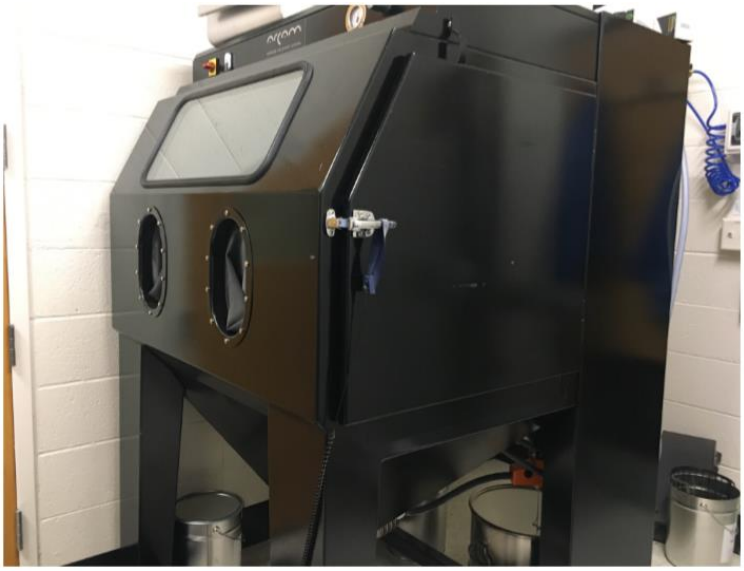

Arcam Powder Recovery System.

C. Testing Equipment

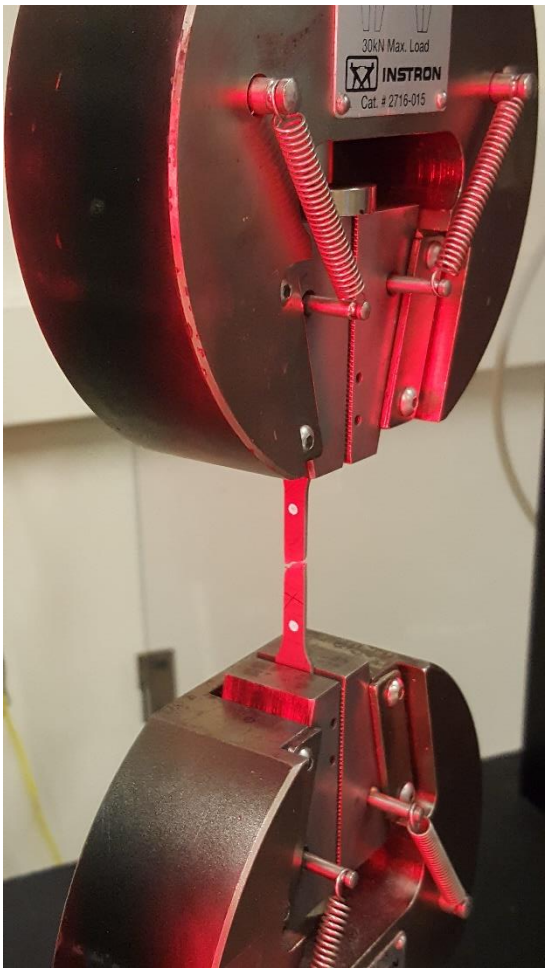

Instron load frame equipped with 50 kN load cell, 30 kN wedge grips, and an optical extensometer.

Keyence VR-3100. Non-contact 3D imager used for profilometry.

D. Powder Chemistry

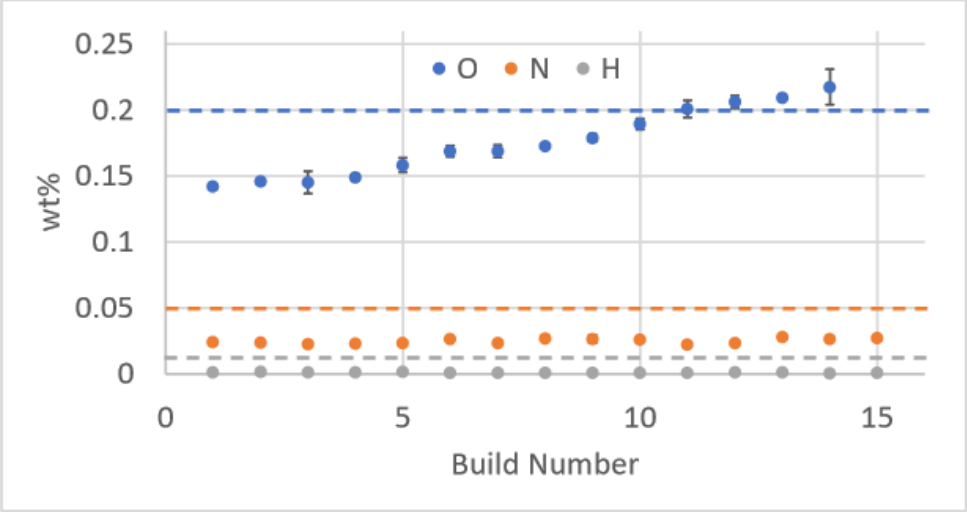

O, N and H content obtained by Sean Ghods using inert gas fusion courtesy of Boeing Everett.

E. Particle Size Distribution

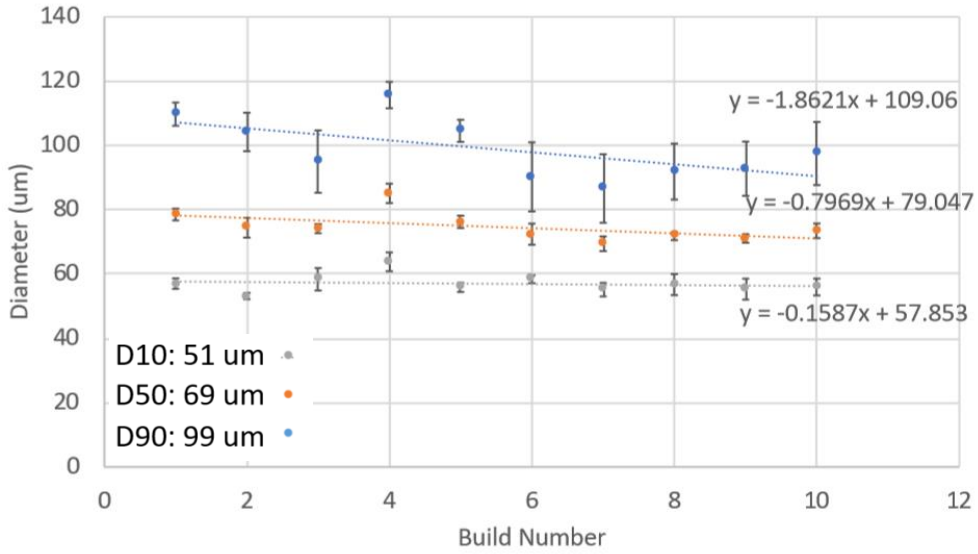

D10, D50, D90 particle size diameters against build number, including the values at build 10. Obtained by Sean Ghods using light scattering techniques.

F. Microstructure

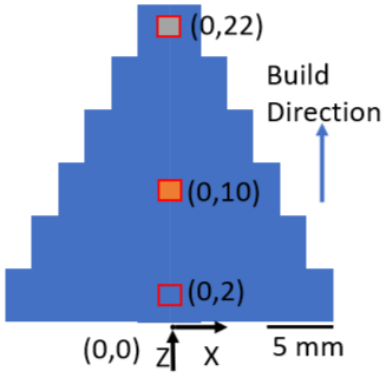

Diagram indicating locations of microstructural evaluation on a cylindrical pyramid.

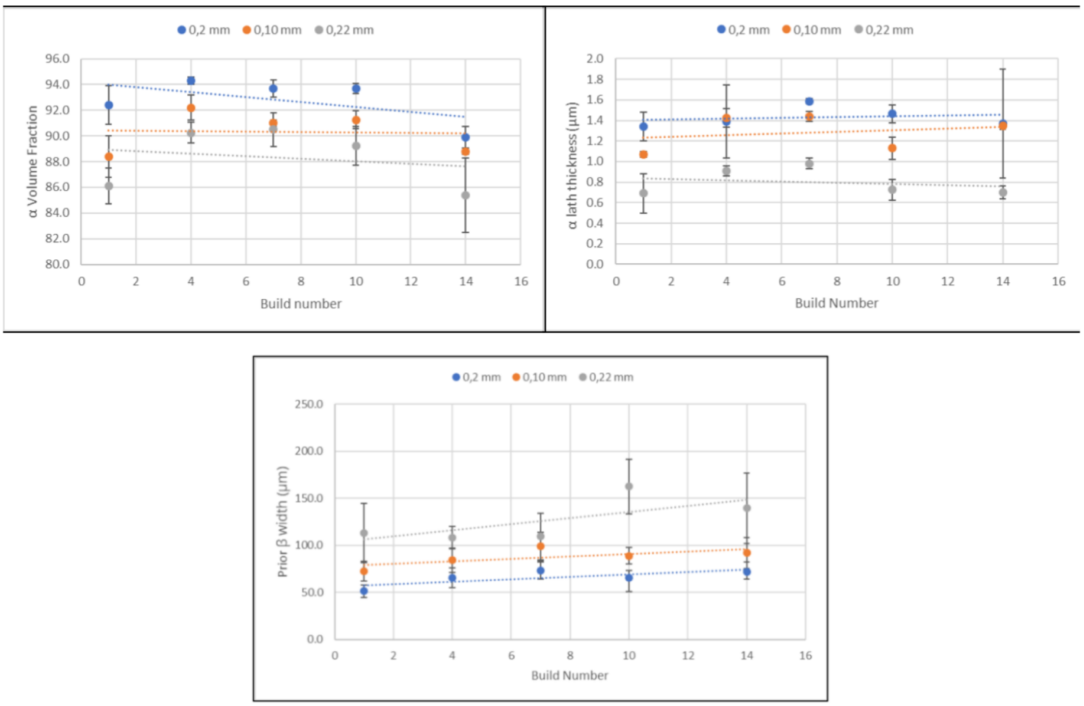

α volume fraction, α lath thickness, and prior β width against build number obtained by Eric Schultz.

G. Void Volume Fraction

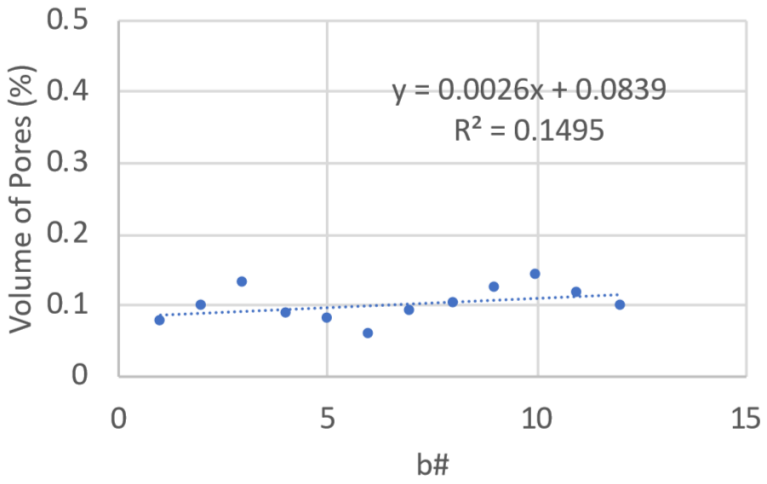

Volume fraction of pores present in the designated micro-CT sample. Obtained by Sean Ghods using micro-CT.

Works Cited

[1] A. Safdar, L. Y. Wei, A. Snis, and Z. Lai, “Evaluation of microstructural development in electron beam melted Ti-6Al-4V,” *Mater. Charact.*, vol. 65, no. Dld, pp. 8–15, 2012.

[2] ASTM Int’l, “F1472 - 14: Standard Specification for Wrought Titanium-6Aluminum-4Vanadium Alloy for Surgical Implant Applications (UNS R56400),” pp. 1–5.

[3] ASTM Int’l, “ASTM F2924 - 14: Standard Specification for Additive Manufacturing Titanium-6 Aluminum-4 Vanadium with Powder Bed Fusion,” vol. i, pp. 1–9, 2014.

[4] Arcam AB, “Arcam-Ti6Al4V-Titanium-Alloy.”

[5] S. Kalpakjian and S. Schmid, *Manufacturing Processes for Engineering Materials*, 5th ed. Pearson Education, 2008.

[6] ASTM Int’l, “ASTM E8M - 16a: Standard Test Methods for Tension Testing of Metalic Materials,” pp. 1–30, 2018.

[7] T. DebRoy *et al.*, “Additive manufacturing of metallic components – Process, structure and properties,” *Progress in Materials Science*. 2018.

[8] K. Darvish, Z. W. Chen, and T. Pasang, “Reducing lack of fusion during selective laser melting of CoCrMo alloy: Effect of laser power on geometrical features of tracks,” *Mater. Des.*, vol. 112, pp. 357–366, 2016.

[9] J. T. Tuomi *et al.*, “In vitro cytotoxicity and surface topography evaluation of additive manufacturing titanium implant materials,” *J. Mater. Sci. Mater. Med.*, vol. 28, no. 3, p. 53, Mar. 2017.

[10] P. Wang *et al.*, “Effects of Processing Parameters on Surface Roughness of Additive Manufactured Ti-6Al-4V via Electron Beam Melting,” *Materials (Basel).*, vol. 10, no. 10, p. 1121, Sep.

2017.

[11] D. Gu and Y. Shen, “Balling phenomena in direct laser sintering of stainless steel powder: Metallurgical mechanisms and control methods,” *Mater. Des.*, vol. 30, no. 8, pp. 2903–2910, Sep. 2009.

[12] M. Svensson, U. Ackelid, and A. Ab, “Titanium Alloys Manufactured with Electron Beam Melting Mechanical and Chemical Properties,” *Proc. Mater. Process. Med. Devices Conf.*, pp. 189–194, 2010.

[13] X. Tan *et al.*, “Graded microstructure and mechanical properties of additive manufactured Ti–6Al–4V via electron beam melting,” *Acta Mater.*, vol. 97, pp. 1–16, Sep. 2015.

[14] C. de Formanoir, S. Michotte, O. Rigo, L. Germain, and S. Godet, “Electron beam melted Ti-6Al-4V: Microstructure, texture and mechanical behavior of the as-built and heat-treated material,” *Mater. Sci. Eng. A*, 2016.

[15] B. J. Hayes *et al.*, “Predicting tensile properties of Ti-6Al-4V produced via directed energy deposition,” *Acta Mater.*, vol. 133, pp. 120–133, 2017.

[16] P. Castany, F. Pettinari-Sturmel, J. Douin, and A. Coujou, “In situ transmission electron microscopy deformation of the titanium alloy Ti-6Al-4V: Interface behaviour,” 2007.

[17] X. Wang and K. Chou, “EBSD study of beam speed effects on Ti-6Al-4V alloy by powder bed electron beam additive manufacturing,” *J. Alloys Compd.*, pp. 236–244, 2018.

[18] H. Conrad, “Effect of interstitial solutes on the strength and ductility of titanium,” *Prog. Mater. Sci.*, vol. 26, no. 2–4, pp. 123–403, 1981.

[19] H. P. Tang, M. Qian, N. Liu, X. Z. Zhang, G. Y. Yang, and J. Wang, “Effect of Powder Reuse Times on Additive Manufacturing

of Ti-6Al-4V by Selective Electron Beam Melting," *JOM*, vol. 67, no. 3, pp. 555–563, Mar. 2015.

[20] N. Hrabe and T. Quinn, "Effects of processing on microstructure and mechanical properties of a titanium alloy (Ti-6Al-4V) fabricated using electron beam melting (EBM), part 1: Distance from build plate and part size," *Mater. Sci. Eng. A*, 2013.